1

Thermodynamics and Kinetics of Quantum Dot Growth

Vitaly Shchukin, Eckehard Schöll, and Peter Kratzer

Abstract. Basic processes responsible for the formation of quantum dot (QD) nanostructures occur on a large range of length and time scales. Understanding this complex phenomenon requires theoretical tools that span both the atomic-scale details of the first-principles methods and the more coarse-scale continuum approach. By discussing the time scale hierarchy of different elementary kinetic processes we emphasize several levels of constraint equilibrium of the system and elucidate pathways to reach corresponding stable or metastable states. Main focus is given to the InAs/GaAs material system which is the most advanced one for applying QDs in optoelectronics. First principles calculations of the potential energy surfaces by the density functional theory (DFT) gain the knowledge about potential minima corresponding to the preferred adsorption sites and barriers that govern the rates of diffusion, desorption, and island nucleation in both unstrained and strained systems. Based on these ab initio parameters, kinetic Monte Carlo (kMC) simulations have allowed a detailed theoretical description of GaAs/GaAs and InAs/InAs homoepitaxial growth and elucidated the nucleation and evolution of InAs islands on GaAs. A hybrid approach combining DFT calculations of the surface energies and continuum elasticity theory for the strain relaxation energy has given the equilibrium shape of InAs/GaAs QDs as a function of volume and explained the observed shape transitions. For the ensembles of strained QDs, the Fokker-Planck evolution equation has explained the formation of different types of metastable states in sparse and dense arrays, and the kMC simulations have proposed a tool to distinguish kinetically controlled and thermodynamically controlled QD growth. By continuum elasticity theory in elastically anisotropic semiconductor systems, transitions between vertically correlated and vertically anticorrelated growth of QD stacks has been explained, and yet another approach has been proposed to control the formation of complex nanoworlds.

1.1 Introduction

Data transmission, processing and storage form the backbone of the modern information society. At the beginning of 1990s, a few outstanding discoveries concerning self-organization phenomena on crystal surfaces marked a change of major paradigms in semiconductor physics and technology. The new approach in epitaxy enables fast parallel fabrication of large densities of quantum dots and wires for almost unlimited material combinations and has become the basis for the powerful new branch of nanotechnology [1, 2].

Quantum dots (QDs), nanometer-scale coherent inclusions showing a discrete atom-like electronic spectrum up to room temperature and above, have major advantages for applications as an active medium of optoelectronic devices. These properties have already resulted in many breakthroughs in the field of semiconductor lasers. QD lasers, based on the most-studied three-dimensional In(Ga)As/GaAs QDs, have shown superior performance with respect to conventional quantum well lasers regarding the following parameters [3, 4]: *i*) higher characteristic temperature T_0 referring to the thermal stability of the threshold current density; *ii*) higher robustness against structural defects; *iii*) better beam quality and effective suppression of filamentation, etc. Combining self-organization phenomena and nanoengineering, including a defect-reduction technique that enables selective elimination of dislocated QDs [4, 5], has allowed fabrication of top performance GaAs-based QD lasers for the practical 1300 nm spectral range. Further advances in nanoengineering include a defect-reduction technique in thick metamorphic layers that has allowed blocking the propagation of extended defects in the GaInAs films grown on GaAs substrates to the upper layers. This enables fabrication of high-performance degradation-robust InAs/GaInAs QD lasers for the spectral range of 1460–1500 nm [6–8]. Using two-dimensional InAs/GaAs QDs obtained in the submonolayer deposition mode results in an ultra-high volume density of QDs. This method enables the ultrahigh frequency (20 GB/s) thermally insensitive (up to 85°C) operation of a vertical cavity surface emitting laser (VCSEL) [9–11].

A complementary field of exciting QD applications requires, on the contrary, an ultra-low QD density which allows access to single dots. The QD-based sources of linearly polarized single photons [12, 13] as well as a source of entangled photons [14] have been realized. These sources form an element basis for the emerging field of quantum cryptography and have potential use in future quantum computing systems.

The progress in the area of epitaxial nanostructures and, in particular, the development of quantum dot- and quantum wire-semiconductor technology employing self-organization phenomena requires a profound understanding of the basic physics behind the spontaneous formation of nanostructures. The progress can only be reached and has been actually reached by combined efforts in

(i) Designing growth experiments
(ii) Developing theory of spontaneous nanostructuring
(iii) Performing precise structural and optical characterization of the grown objects

(iv) Developing experimental tools that allow for controlling and tuning of geometrical parameters and electronic spectra of the nanostructures
(v) Optimizing growth techniques to meet device requirements; and
(vi) Fabricating novel nanostructure-based devices that, in fact, fuel the research area

1.1.1 Length and Time Scales

This chapter focuses on the theoretical modeling of the basic processes responsible for the formation of QD nanostructures. The processes underlying nanostructure formation occur over a large range of length and time scales. One can mention deposition/evaporation of atoms on/from the surface, chemical reactions, diffusion hopping of adatoms over the surface, nucleation of islands, attachment/detachment of adatoms to/from islands, evolution of an island ensemble towards equilibrium/ripening, intermixing/segregation, etc.

A complete understanding of the behavior of materials requires theoretical tools that span both the atomic-scale details of the first-principles methods and the more coarse-grained description by a continuum approach. An overview of various computational strategies focused on combining traditional methods—density functional theory,
molecular dynamics, Monte Carlo (MC) methods and continuum description—within a unified multiscale approach is given in [15].

Figure 1.1(a) illustrates physical times and sizes of QD nanostructures that are accessible by different methods within $t_c = 24\,\mathrm{h}$ computational time of a central processor unit of a computer (CPU time). Within an overall CPU time of t_c one can perform n steps of CPU time τ_c, and thereby advance the physical time by t_p in steps of the physical time increment τ_p, i.e. $t_c = n\tau_c$ and $t_p = n\tau_p$. The best known scaling of the numerical effort with the number of atoms N is linear (see, e.g. [16]). The physical time reachable in a given CPU time for a system with characteristic length L and characteristic density $\rho = N/V = NL^{-3}$ is then

$$t_p = Ct_c\tau_p \cdot L^{-3}, \tag{1.1}$$

with a prefactor C depending on the underlying method for the force evaluation. Different gray levels in Fig. 1.1(a) indicate accessible time scales and sizes that can be modeled by *ab initio* molecular dynamics, or many-body potential (MBP) molecular dynamics, or by *ab initio* or MBP kinetic Monte Carlo (kMC) simulations. The regime of continuum-elasticity theory (CET) is shown as being independent from the physical time as it is primarily a static approach.

Apart from computational feasibility, one should emphasize that each of the theoretical tools has its own advantages. Thus, *ab initio* methods give an exact ultimate answer for a given materials system. On the other hand, continuum theory is able to describe different material systems on a coarse scale, predicting different scenarios that depend on the material parameters. A multiscale modeling of nanostructure formation allows us to combine the advantages of several of the more traditional methods.

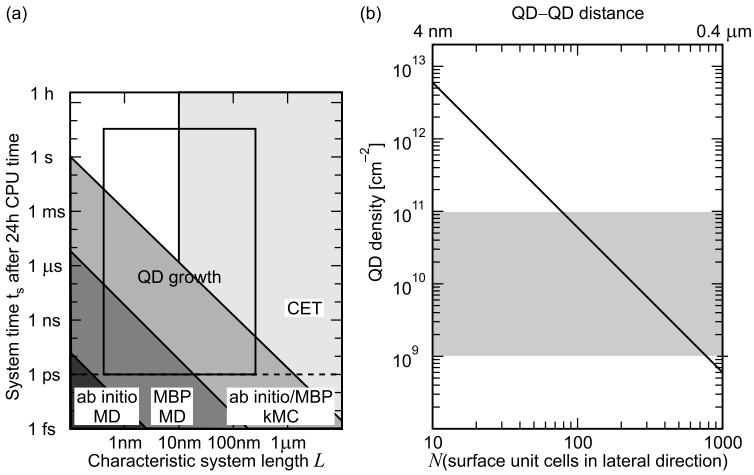

Fig. 1.1. Physical times and sizes of QD nanostructures that are accessible by different methods within a CPU time of $t_c = 24\,\mathrm{h}$ and a time increment of $\tau_p = 1\,\mathrm{fs}$ (**a**). The computational effort of a typical relaxation with a many-body potential is indicated by a dashed line. The regions of QD growth (rectangle) can be deduced from the experimentally observed QD densities (*gray area* in (**b**)), the relation between QD density and QD–QD distance is shown by a solid line in (**b**), and the reported typical formation times of a few seconds. From [16], with permission

1.1.2 Multiscale Approach to the Modeling of Nanostructures

For assessing the thermodynamic stability of semiconductor nanostructures in various stages during their preparation, the thermodynamics of semiconductor surfaces is obviously a very important factor. In this context it is important to emphasize several levels of partial, or *constraint equilibrium*. For example, if the diffusion of atoms over the island facets is faster than the attachment/detachment of adatoms to/from an island, an island can form an *equilibrium island shape* at a given volume. On the time scale where attachment/detachment processes are fast, and migration of adatoms between the islands is slow, a *local surface equilibrium* between an island and the wetting layer (adatom sea) can form. On the time scale where material exchange between islands mediated by the wetting layer occurs, the system evolves towards a *global surface equilibrium* provided the deposition is stopped (growth interruption); evaporation of atoms and intermixing/segregation processes which would occur via bulk migration are negligible.

Most semiconductor surfaces are reconstructed, therefore first-principles calculations using realistic atomic structures are crucial to gain knowledge about the surface free energies and surface stresses of the surfaces and interfaces that are being formed. In the preparation of self-assembled quantum dots by Stranski–Krastanow growth, examples are the wetting layer, the interfaces between a quantum dot and the capping layer, or the side facets of free-standing quantum dots. By combining density-functional theory (DFT) calculations using detailed surface atomic structure

with thermodynamic considerations, i.e. by *ab initio* thermodynamics, valuable insight can be gained into the thermodynamics of surface and interface formation.

As a basis for the understanding of possible kinetic limitations that could occur during the growth of quantum dots, it is important to have detailed information not only about thermodynamics, but also about the growth kinetics, both of pure semiconductors and heterostructures. For applying quantum dots in optoelectronic devices, InAs/GaAs is the most advanced material system where numerous experiments have been performed and suitable growth conditions are best understood. Therefore most of the theoretical work presented in the following focuses on this system. Understanding growth kinetics from an atomistic perspective starts with DFT calculations of potential-energy surfaces (PESs) for the relevant molecular processes. From the PES, knowledge can be gained both about the energy minima corresponding to the preferred adsorption sites of Ga or In atoms or arsenic molecules, as well as knowledge about the energy barriers that govern the rates of diffusion, desorption and island nucleation. For homoepitaxy of GaAs on a GaAs(001) substrate, an extensive set of DFT calculations has been performed in order to obtain these data. Although the heteroepitaxial system InAs/GaAs is clearly much more complicated to describe on the atomic level, in this case the atomistic approach using DFT calculations has succeeded in elucidating several structures and processes relevant to quantum dot growth.

1.2 Atomistic Aspects of Growth

1.2.1 Diffusion of Ga Atoms on GaAs(001)

For epitaxy on the frequently used GaAs(001) substrate, the most important surface reconstructions are the $\beta 2(2 \times 4)$ and the $c(4 \times 4)$ reconstructions. These are most stable under the moderately arsenic-rich or very arsenic-rich conditions typical for molecular beam epitaxy at 500–600°C and 400–500°C, respectively. For Ga adatom diffusion on the GaAs(001)$\beta 2(2 \times 4)$ surface, density-functional theory calculations [17] have shown that the surface diffusion is highly anisotropic, with energy barriers of 1.2 eV and 1.5 eV in the $[\bar{1}10]$ direction (along the trenches) and the [110] direction, respectively. Remarkably, this study showed that Ga adatoms are able to split the surface arsenic dimers that are part of the $\beta 2(2 \times 4)$ reconstruction, and find their most favorable binding sites in this position. The same holds true for In adatoms on various (001) surfaces [18, 19]. However, other binding sites for In (outside As dimers) exist that are more favorable. For both Ga or In deposition, the ability of these adatoms to break up As dimers is an important atomistic step for growth on arsenic-rich (001) surfaces. Figure 1.2 shows, for the case of In/GaAs(001)$c(4 \times 4)$, the potential energy surface that governs the insertion of the In atom into an As dimer.

1.2.2 Energetics of As_2 Incorporation During Growth

In molecular-beam epitaxy (MBE), both As_4 or As_2 molecules (obtained by cracking As_4) can be used as sources of arsenic. Density-functional theory calculations

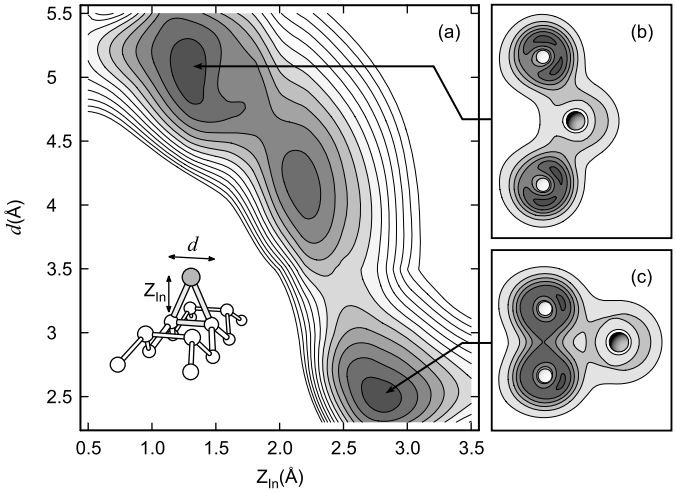

Fig. 1.2. (**a**) Binding energy of an In adatom interacting with the center As dimer in the GaAs(001)$c(4 \times 4)$ reconstruction as a function of the As–As distance d and the In height above the midpoint of the dimer z_{In}, as indicated in the inset. (**b**, **c**) Bonding configuration and valence electron density in the plane containing the In adatom and the As dimer for two minima of E_b

performed for the case of As_2 have shown that As_2 molecules bind only weakly on perfect GasAs(001)$\beta 2(2 \times 4)$ or GaAs(001)$c(4 \times 4)$ surfaces. A similar behavior is expected for As_4 molecules, since they are less reactive than As_2. According to these DFT calculations [20, 21], the As_2 molecules find sufficiently strong binding sites (binding energy $>$ 1.5 eV) only after overcoming high energy barriers, or if additional Ga adatoms are already present on the surface, e.g. from previous Ga deposition. The latter finding is in accordance with the experimental observation that the sticking coefficient of an As_2 molecular beam on GaAs(001)$\beta 2(2 \times 4)$ is measurably different from zero only if a Ga evaporation source is operative at the same time [22].

1.2.3 Kinetic Monte Carlo Simulation of GaAs Homoepitaxy

The data about binding energies of Ga adatoms and As_2 molecules and the energy barriers for desorption, diffusion and island nucleation obtained from the DFT calculations were combined in a kinetic Monte Carlo (kMC) study of GaAs homoepitaxy [23]. With this technique, it is possible to overcome the huge gap between the time scales of molecular processes (picoseconds) and the relevant time scales for growth experiments (several seconds up to minutes). As a result of these simulations, it was possible to predict the GaAs island density as a function of temperature and flux [23, 25, 26]. Particularly advantageous is the adatom-density kinetic Monte Carlo method [27] that speeds up the simulations for large sample areas.

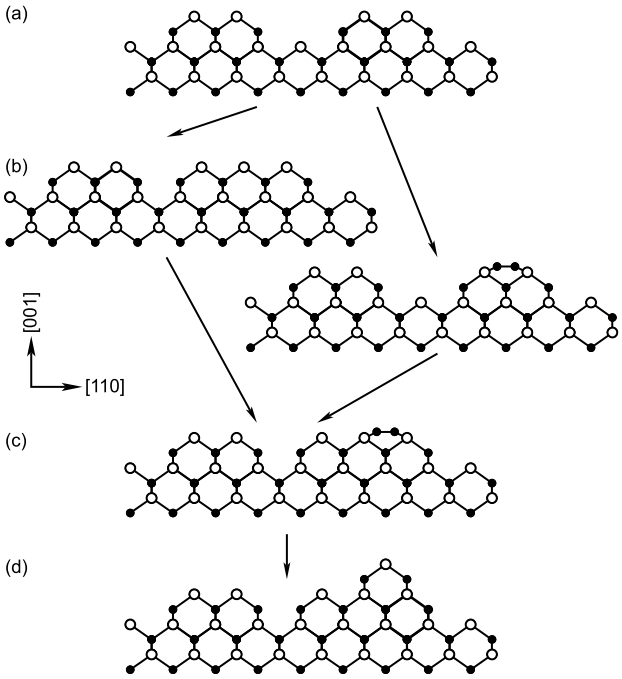

Fig. 1.3. Schematic representation of the growth mechanism in GaAs homoepitaxy on the GaAs(001)-$\beta 2$ surface (*side view*). (**a**) The substrate is corrugated on the atomic scale, with "hills" of As dimers (*open circles*, *dimer axis perpendicular to the plane of the graph*) and "trenches". Ga atoms (*filled circles*) with dangling bonds appear at the "sidewalls" of the trenches. (**b**) Left: Attachment of material in the trench, yielding a local $\beta 1$-reconstruction; right: Ga dimer as a metastable growth intermediate. (**c**) Formation of a Ga dimer adjacent to locally filled trench. (**d**) The island extends into a new layer after As_2 adsorption

With the kMC simulations, we managed to pinpoint a sequence of processes that give rise to island growth on the GaAs(001)-$\beta 2$ substrate [23]. Some metastable intermediates are shown in Fig. 1.3. By attachment of material in the trenches of the $\beta 2$-reconstruction, two Ga atoms are incorporated into the surface, and a third As dimer is added to the two top-level As dimers of the $\beta 2$-reconstruction, yielding a unit cell with local $\beta 1$-reconstruction (Fig. 1.3(b), left part). If the rate of desorption of arsenic exceeds the rate of adsorption (i.e., when growing at high temperatures and under low As fluxes), mobile Ga adatoms may agglomerate into Ga dimers (Fig. 1.3(b), right part). The formation of these Ga dimers occurs preferentially near sites where material has already filled the trenches, i.e., where the local $\beta 1$-reconstruction has appeared (Fig. 1.3(c)). Finally, if two or more such Ga dimers have formed at sites adjacent in the $[\bar{1}10]$ direction, these offer favorable adsorption sites for As_2 molecules. Adsorption of As_2 on these sites results in a small island that extends into a new layer (Fig. 1.3(d)). Experimental studies in combination with modeling have demonstrated that these islands, once they grow larger, redevelop the

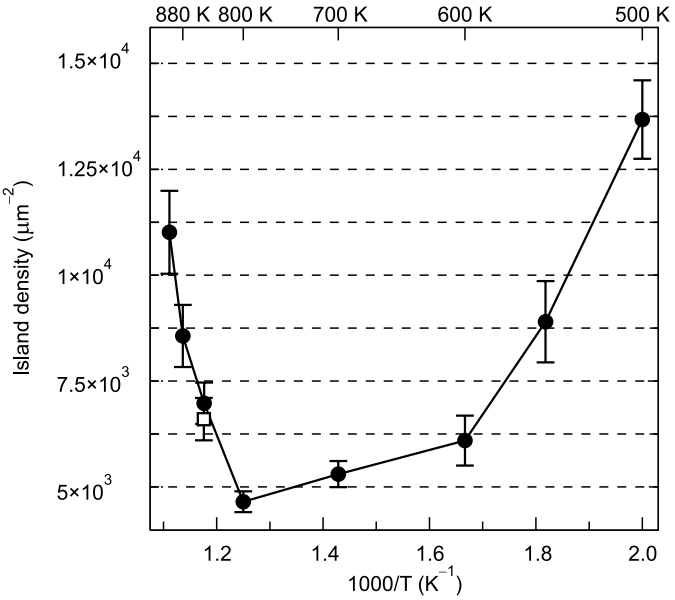

Fig. 1.4. Island number density for GaAs homoepitaxy after deposition for 1 s, using a Ga flux of 0.1 ML/s and an effective As_2 flux of 100 ML/s. (This rather high value is used to take into account the effect of multiple bounces of As_2 molecules on the surface.) The filled circles are results of kMC simulations ([23]), the open square symbol is the measured island density from [24], at a Ga flux of 0.1 ML/s and a (direct) As_2 flux of 0.8 ML/s

well-known $\beta 2$-reconstruction pattern [28]. As a result of this growth mechanism, such islands are elongated along the $[\bar{1}10]$ direction. One can get a good idea about a typical growth sequence by looking at animated snapshots taken in millisecond time intervals of the atomic configurations obtained from the kMC simulations. Such a "movie" is available from the Web [29].

Already after depositing a fraction of a monolayer of GaAs, the island density reaches a saturation value. At the most frequently used growth temperature of 580°C, the kMC simulations predict an island density of 7×10^{11} cm^{-2}, in good agreement with experiments using molecular beam epitaxy followed by an analysis of the island density in scanning tunneling microscopy images, yielding 6.6×10^{11} cm^{-2}, see [24, 30]. Simulations of hypothetical growth at widely different temperatures, 500 K $< T <$ 900 K, assuming that the $\beta 2$-reconstruction could be stabilized over the whole temperature range, show a remarkable temperature dependence of the island density (see Fig. 1.4). While at low temperature the island density decreases with increasing temperature, as expected from nucleation theory, the experimentally relevant growth regime is on the rising slope of the island density at high growth temperatures. This growth regime is a unique feature of a two-component system: At $T \sim 800$ K, desorption of As_2 sets in; therefore the attachment of material to the edges of existing islands (that requires permanent arsenic incorporation) becomes reversible above this

temperature. This leads to the observed change in growth kinetics and to an increase in the nucleation of new islands with increasing temperature [23, 26]. Around its minimum at ~800 K, the island density in the kMC simulations is found to be an increasing function of As_2 flux, again in agreement with experiment [24].

In a similar spirit, kMC simulations were performed for the interaction of As_2 with the InAs(001) surface, and for island growth in homoepitaxy on InAs(001). Interestingly, the (2 × 4)-reconstructed InAs(001) surface undergoes a reversible phase transition between the $\beta 2(2\times4)$ and the $\alpha 2(2\times4)$ reconstruction as a function of both temperature and arsenic flux [31, 32]. Both experiment and kMC simulations find that the saturation island density after deposition of a fraction of a monolayer is slightly lower for InAs as compared to GaAs. While InAs epitaxy is done at a lower substrate temperature compared to GaAs epitaxy, the effect of temperature is overcompensated by the generally lower energy barriers for In atoms, and higher rate constants for both In diffusion and As_2 desorption on InAs(001). Despite the strong similarities between InAs and GaAs, there are some differences in details of the growth scenario: For InAs, the island density in InAs homoepitaxy was found to be a decreasing function of As_2 flux (from $5.6 \times 10^{11}\,\mathrm{cm}^{-2}$ to $2.5 \times 10^{11}\,\mathrm{cm}^{-2}$), both in experiments and in kMC simulations [33].

For the self-assembled growth of quantum dots, heteroepitaxy of InAs on GaAs is most relevant. Therefore, it is important to discuss whether the findings for homoepitaxy are transferable to the situation in heteroepitaxy. Experimentally, it has been demonstrated that MBE growth of InAs on the GaAs(001)-$\beta 2(2 \times 4)$ substrate can be performed in such a way that the resulting morphology of two-dimensional (2D) islands is qualitatively similar to homoepitaxy of GaAs [34, 35]. However, this submonolayer growth regime is not typical for quantum dot growth, because the latter requires deposition of 1.5 to 3 monolayers (ML) of InAs. For deposition of 1 ML of InAs or more, a wetting layer with a surface reconstruction substantially different from the substrate is formed (see Sect. 1.2.4). Furthermore, not all of the 2D islands develop into quantum dots, since typically observed quantum dot densities (between $10^{10}\,\mathrm{cm}^{-2}$ and $10^{11}\,\mathrm{cm}^{-2}$) are about one order of magnitude lower than the nucleation density of the 2D islands (between $10^{11}\,\mathrm{cm}^{-2}$ and $10^{12}\,\mathrm{cm}^{-2}$). Nevertheless, it has been found experimentally that the scaling properties of island size distributions carry over from 2D to 3D island formation driven by heteroepitaxial strain [36–38]. While such a scaling behavior is supported by theoretical arguments for 2D islands, the reason for its validity for the 3D case is not yet fully understood by theory.

1.2.4 Wetting Layer Evolution

For MBE growth of InAs quantum dots on GaAs, typically somewhat lower temperatures (400–550°C) are used than for homoepitaxy of GaAs (550–600°C). Under the commonly used As flux, the $c(4 \times 4)$ reconstruction of GaAs(001) appears. The energy barriers for diffusion of single Ga [39] or In [18] atoms on this surface have been determined by density-functional theory. It is found that surface diffusion is close to being isotropic, with energy barriers of 0.94 eV for Ga and 0.67 eV for In atoms.

However, small amounts of In deposited on GaAs(001)$c(4\times4)$ strongly affect the surface morphology. First "incomplete" $c(4 \times 4)$ reconstruction patterns develop, in which part of the As atoms in the surface As dimers are replaced by cations [40–42], followed by a new phase that starts developing at surface steps [43]. Upon further In deposition, the formation of a wetting layer with both commensurate and incommensurate (1×3) and (2×3) reconstruction patterns has been observed by reflection high-energy electron diffraction (RHEED) measurements [44].

Since growth of InAs quantum dots on GaAs(001) proceeds in the presence of this wetting layer, it is important to understand its atomic structure and the thermodynamic driving force for its formation. With the help of DFT calculations, it is possible to investigate the formation energy of the wetting layer as a function of its thickness (= indium deposition) and of variations of the growth conditions. The latter are reflected in the calculations by the choice of the arsenic chemical potential μ_{As}. Both a segregated film of pure InAs, with either $\beta2(2 \times 4)$ or $\alpha2(2 \times 4)$ reconstruction, and formation of an alloyed wetting layer have been considered. For the latter alternative, an As-terminated (2×3) reconstruction was selected, motivated by X-ray diffraction experiments [45] on $\mathrm{In}_x\mathrm{Ga}_{1-x}\mathrm{As}$ surface alloy films that observe this reconstruction at $x = 2/3$, along with a triple-period ordering of In and Ga on the cation sublattice sites. For very As-rich conditions, as shown in Fig. 1.5, the alloyed (2×3)-reconstructed wetting layer is found to be most favorable. Both for less As-rich conditions and thicker films, the $\alpha2(2 \times 4)$ reconstruction is found to be lower in energy, and to extend its range of stability at the expense of the (2×3) reconstruction. The $\beta2(2 \times 4)$ reconstruction that had been studied previously [46, 47]

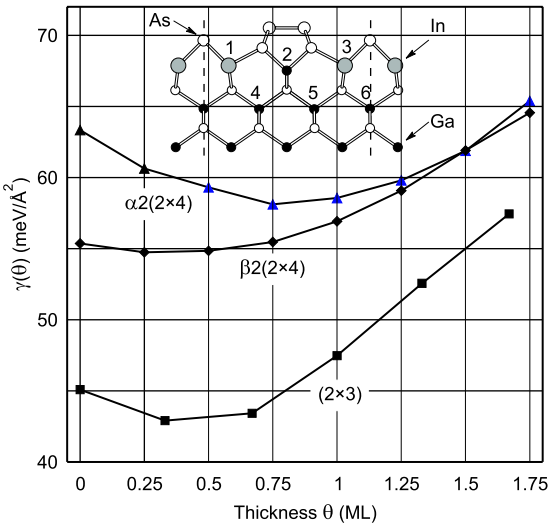

Fig. 1.5. Formation energy γ_{f} of the InAs wetting layer on GaAs as a function of indium deposition θ at very arsenic-rich conditions, $\mu_{\mathrm{As}} = \mu_{\mathrm{As(bulk)}}$. The inset shows the cation sites included in the calculation of $\gamma_{\mathrm{f}}(\theta)$ for the (2×3) structure

is found to occur in an intermediate regime of moderately As-rich conditions. The strain energy stored in the wetting layer in all cases shows up as a linear increase of the formation energy with the thickness, as seen in Fig. 1.5.

1.3 Size and Shapes of Individual Quantum Dots

1.3.1 Hybrid Approach to Calculation of the Equilibrium Shape of Individual Quantum Dots

While quantum dots display electronic properties different from bulk materials due to the confinement of electrons and holes on the nanometer scale, their structural and elastic properties are less affected by the physics on the nanoscale. Typical InAs quantum dots of 10 nm to 20 nm base length consist of the order of 10^4 atoms. If an InAs island of this size is grown pseudomorphically on GaAs, the elastic energy introduced both in the island and in the substrate due to the mismatch of the lattice constants of the two materials can be well described by classical elasticity theory. Deviations from the classically expected behavior, e.g. due to surface stress, are limited to relatively small regions of space and can be treated separately if required. This can be done, e.g., by taking into account modifications of the surface energies due to surface stress. Therefore it is possible to separate the total energy associated with the formation of strained free-standing islands into the energy gain from partial strain relief, and the energy cost due to the formation of side facets and edges. Knowing the total formation energy, the shape of such an island can be determined under the assumption of thermal equilibrium, by minimizing the formation energy for a fixed amount of material in the island.

In order to calculate the contributions to the formation energy, a hybrid approach has been devised [48, 49] that allows us to employ specific methods most suitable for calculating each contribution separately. The energy gain due to strain relaxation is calculated according to continuum elasticity theory, e.g. by a finite-element method, while surface energies and surface stresses are calculated using density functional theory. The edge energies can be estimated from DFT calculations as well. They become less important for larger islands, and have therefore been neglected in most studies.

Applying the hybrid approach, the equilibrium quantum dot shape has been determined for InAs on GaAs(001) [48, 49], using low-index facets as boundaries of the InAs islands (see Fig. 1.6(a)). A similar study was performed for InP quantum dots on GaP(001) [50]. These studies showed that the equilibrium shape of quantum dots depends both on the chemical environment during quantum dot growth, and on the size of the dots. For InAs quantum dots grown on GaAs, the shapes predicted by the hybrid approach for very arsenic-rich growth conditions are shown in Fig. 1.6(c,d). For example, the InAs($\bar{1}\bar{1}\bar{1}$) facet, for which a low-energy As-rich reconstruction exists, becomes very prominent in the quantum dot shape for As-rich conditions (see Fig. 1.6(c,d)). The equilibrium shape results from an optimization process that allows us to continuously change the shape (and thus the fraction of total surface area

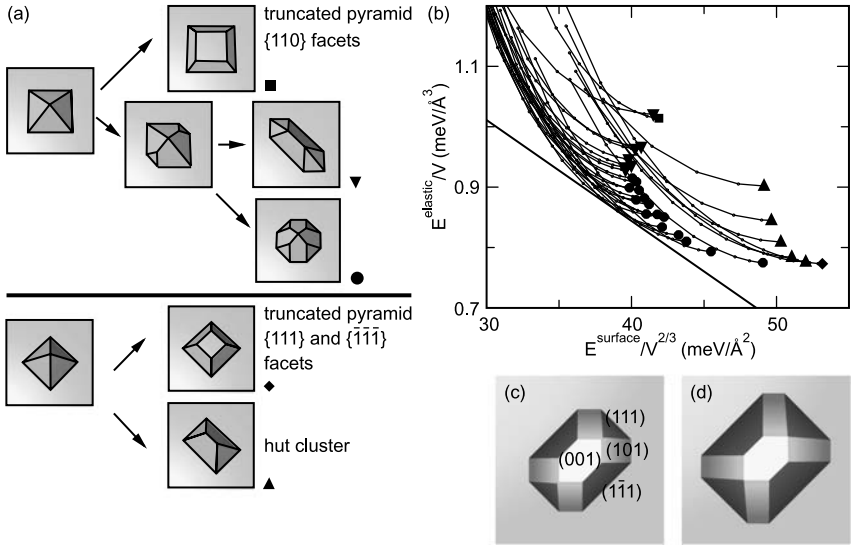

Fig. 1.6. (**a**) Island shapes for InAs quantum dots on GaAs considered in [49], consisting of low-index facets. The basic shapes are pyramids oriented in two different ways relative to the substrate. Further shapes are generated by cutting off the top of the pyramid, or by cutting off the apices at its base, leading to multifaceted islands. (**b**) The elastic energy per volume E^{elastic}/V versus the surface energy per area $E^{\text{surface}}/V^{2/3}$ for InAs islands. The symbols refer to the shapes displayed in (**a**): Square: square-based pyramid with four $\{101\}$ facets. Diamond: square-based pyramid with two $\{111\}$ and two $\{\bar{1}\bar{1}\bar{1}\}$ facets. Triangles up: huts with two $\{111\}$ and two $\{\bar{1}\bar{1}\bar{1}\}$ facets. Triangles down: square-based $\{101\}$ pyramids with $\{\bar{1}\bar{1}\bar{1}\}$ truncated edges. Circles: islands with four $\{101\}$, two $\{111\}$, and two $\{\bar{1}\bar{1}\bar{1}\}$ facets. The small dots denote the corresponding truncated islands that are connected by the full lines. The dashed line is the curve of constant total energy $E^{\text{elastic}} + E^{\text{surface}}$ that selects the equilibrium shape for the volume $V = 2.14 \times 10^5$ Å^3. (**c**)–(**d**) The equilibrium shape of a strained coherent InAs island in an As-rich environment at two different volumes, (**c**) $V \approx 2 \times 10^5$ Å^3 ($\sim 10\,000$ atoms), (**d**) $V \approx 4 \times 10^5$ Å^3 ($\sim 20\,000$ atoms). From [49], with permission

contributed by each side facet) as a function of quantum dot size. The principle of the optimization process is illustrated in Fig. 1.6(b). For the balance between the energy gain due to elastic relaxation, and the energy cost of forming the side facets, the size of the quantum dot is crucial: Each quantum dot size corresponds to a straight line with a specific slope in the diagram of Fig. 1.6(b), where the dimensionless elastic energy and the surface energy (both normalized with the appropriate power of the quantum dot volume) are plotted on the axes. Varying the size of a quantum dot with given shape shows up in Fig. 1.6(b) as a curve labeled by a specific symbol. The locus where the straight line becomes tangent to the lower envelope of all curves defines the optimum island shape for a given volume. Larger quantum dots correspond to a smaller slope, and therefore touch the envelope at a different point. While the quantum dots grow, the magnitude of the elastic energy relief (which is proportional to the quantum dot volume) increases more strongly, compared to the surface en-

ergy contribution. Therefore, large quantum dots show a higher aspect ratio (defined as height-to-base ratio) than small ones. The top facet is predicted to contribute a smaller fraction of the overall surface area for the bigger quantum dots. Again, this can be seen by inspecting the equilibrium shapes in Fig. 1.6(c,d).

For InAs quantum dots grown on GaAs, the typically observed shapes have a smaller aspect ratio (between 0.2 and 0.3) compared to the prediction of the hybrid approach for quantum dots bounded exclusively by low-index facets (aspect ratio 0.3 to 0.5). Only for quantum dots grown with an unusually small growth rate at rather high temperatures [51], a shape has been observed that is qualitatively similar to the one theoretically predicted. This can be interpreted as a hint that even the shape of quantum dots is not fully determined by thermal equilibrium for MBE growth of InAs quantum dots under typical conditions. Another indication for a kinetically determined shape comes from InAs quantum dots grown on the GaAs(113) substrate, where very elongated islands have been observed in STM studies [52]. From the (calculated) surface energies of various InAs surface orientations, which deviate only in a range of $\pm 10\%$ from their mean value of $\sim 40\,\mathrm{meV/\AA^2}$, one would not expect the equilibrium shape to be so strongly elongated. On the other hand, the shapes predicted by the hybrid approach in [50] for InP quantum dots were found to be in good agreement with those observed for large MOCVD-grown dots [53].

1.3.2 Role of High-Index Facets in the Shape of Quantum Dots

For a more refined understanding of the shape of quantum dots, knowledge about the atomic structure and surface energies of high-index surfaces turned out to be important, since they play a role as side facets of the quantum dots. With this motivation, both the GaAs(114) [54, 55] and the GaAs(2 5 11) [56, 57] surfaces were investigated in combined experimental and theoretical studies. By growing thin films of GaAs on specially cut wafers, it has been demonstrated that both the (114) and the (2 5 11) surfaces are stable under the conditions of molecular beam epitaxy. Structural models for the As-rich GaAs(2 5 11) reconstruction, and for both the Ga-rich $\omega(2 \times 4)$ [54] and As-rich $\alpha(2 \times 4)$ reconstructions [55] of GaAs(114) were proposed on the basis of STM images. Density-functional theory calculations of the surface energies showed that these reconstructions are indeed low in energy (within their respective range of stability). Analogous results were obtained for InAs by calculating the surface energies for these high-index orientations, see Fig. 1.7(a). Comparing the observed STM images for GaAs with calculated images using the Tersoff–Hamann approach, further support for the proposed structural models could be obtained. While the newly proposed surface reconstructions for the (114) and (2 5 11) surfaces fulfill the electron-counting rule, the calculations also demonstrated that this rule becomes less important if the size of the unit cell of the reconstruction is large. As a result, the (137) and (3 7 15) reconstructions of GaAs and InAs, which are built up from similar structural elements (As dimers, three-fold coordinated As and Ga surface atoms) as the (2 5 11) surface, but do not comply with the electron counting rule, are similarly low in surface energy (see Fig. 1.7(a)).

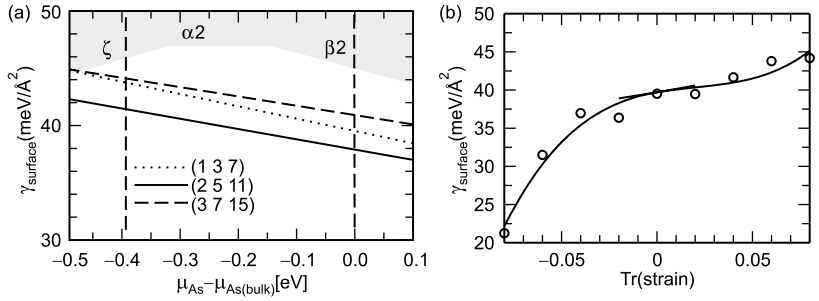

Fig. 1.7. (**a**) Calculated surface energies as a function of the chemical potential of arsenic for the InAs(2 5 11) surface with three As dimers per unit cell (*solid line*), for the InAs(3 7 15) surface with two As dimers per unit cell (*dashed line*), and for the InAs(137) surface with one As dimer per unit cell (*dotted line*). For comparison, surface energies of the InAs(001) $\beta 2(2 \times 4)$, $\alpha 2(2 \times 4)$ and $\zeta(4 \times 2)$, which have the lowest energies of the presently known reconstructions of InAs(001), are indicated by the shaded region. (**b**) Surface energy γ of the InAs(137) surface as a function of strain, ε, per unit surface area (of the unstrained material)

1.3.3 Shape Transition During Quantum Dot Growth

The improved understanding of high-index facets, together with the concept of constrained equilibrium in which the base area occupied by a quantum dots remains fixed during the advanced stages of growth, gave rise to a refined scenario for shape evolution: The quantum dots undergo a shape transition after exceeding a specific size, accompanied by an abrupt drop in the chemical potential for the In adatoms to be incorporated in the dot [58]. In theoretical support of this growth scenario, a detailed discussion of the energetic contributions from elastic relaxation and from the surface energy terms within the hybrid approach has been worked out for the sequence of shapes shown in Fig. 1.8. First, flat islands are formed that are bounded predominantly by high-index facets from the families of {137}, {2 5 11} or {3 7 15} orientations. In accordance with the experimental observations [59], the simplest case of {137} facets is considered in the following. The initial formation of flat islands is also supported by theoretical considerations, since it was shown by a DFT calculation [58] (cf. Fig. 1.7(b)) that the surface energy of InAs(137) is lowered considerably by compressive strain, as is present on the facets of small flat quantum dots. In the course of growth, the occurrence of low-index facets from the {110} and {111} families (that form a steeper angle with the substrate) may become energetically favorable at some point. This is plausible because the steeper quantum dot shape allows for an improved strain relaxation. However, the cost of creating the extra low-index facets pays off only if the quantum dot has already reached a certain minimum size. (Recall that strain relaxation dominates over the surface contributions for large quantum dots.) If we consider the base area of the islands as fixed (which is reasonable since it is a slowly varying quantity), it can be shown that the transition between the island shapes is abrupt. Considering equilibrium among the atoms of an island with the constraint of a fixed base area allows us to define a chemical potential

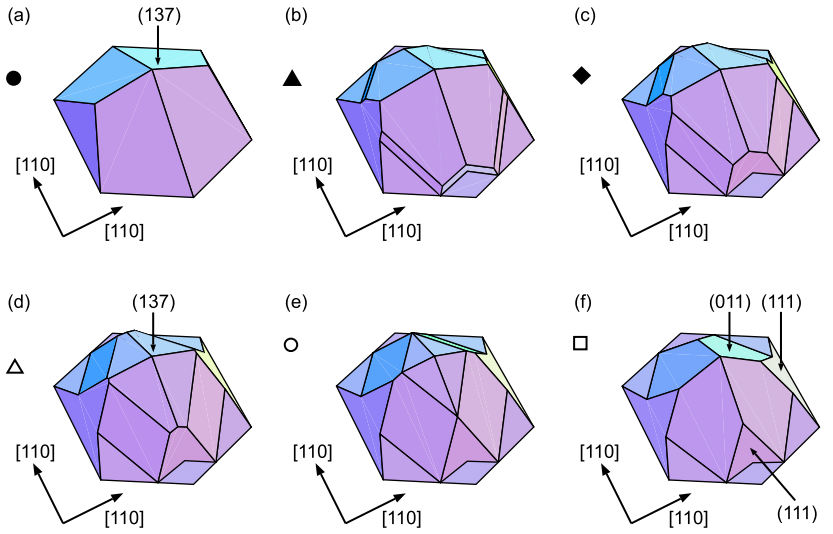

Fig. 1.8. Proposed sequence of shapes for the growth of InAs quantum dots on GaAs(001). Small quantum dots, (**a**), are bounded by {137} and $\{\bar{1}\bar{1}\bar{1}\}$ facets. Growth proceeds mostly through layer-by-layer growth on the {137} facets; however, the newly grown layers do not make contact with the (001) substrate (**b**). As a result, {110} and {111} facets develop at the lower end of the added layers, giving the quantum dot an increasingly steeper appearance (**c**)–(**e**). Eventually, a sharp tip could possibly develop if growth of the {110} facets extends to the top (**f**)

for the In atoms in the island. Since the free energy of the island as a function of island size has a cusp at the volume of the shape transition, the so-defined chemical potential is discontinuous (see Fig. 1.9). The influx of In adatoms from the wetting layer into the quantum dot is driven by the chemical potential difference between the outside and the inside region. For this reason, the discontinuity of the chemical potential has important consequences for the growth kinetics: it has been shown that it leads to so-called anomalous coarsening [60, 61]. As a result, bimodal island size distributions are to be expected, and the width of the smaller size component may be rather narrow. Hence the anomalous coarsening, in addition to the delaying effect of strain on the growth of larger quantum dots (to be described in the following), could explain the frequently obtained narrow size distribution that is desirable for many applications of quantum dots. Moreover, it is noteworthy that the shape evolution suggested by Fig. 1.8 results in an aspect ratio of the islands of ~ 0.3, in satisfactory agreement with the majority of experiments on InAs quantum dots.

1.3.4 Constraint Equilibrium of Quantum Dots with a Wetting Layer

Another important outcome of first-principles calculations was the active role played by the wetting layer during quantum dot growth. The growing quantum dots consume

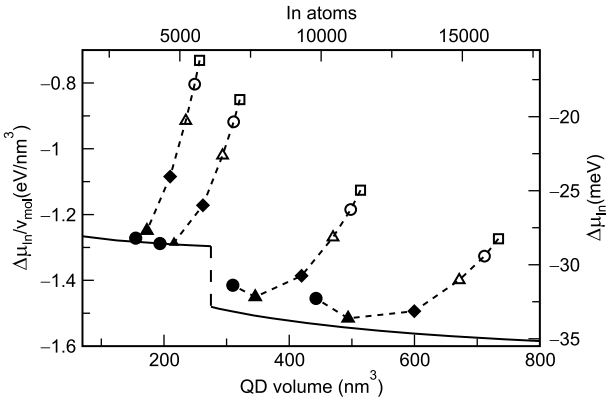

Fig. 1.9. Chemical potential of In atoms in quantum dots of various fixed base areas, as a function of the dot volume. The curves, from upper left to lower right, correspond to quantum dots with a base diameter in [110] direction of 19.8, 24.7, 39.6, and 56.6 nm, respectively. The symbols along the curves refer to the different shapes shown in Fig. 1.8. For quantum dots of small base area, adding material on top of the pyramid (Fig. 1.8(a)) would result in an increase of chemical potential and hence does not occur spontaneously. For quantum dots with a base length larger than 30 nm, however, a transition from the shape Fig. 1.8(a) to Fig. 1.8(b) becomes a spontaneous process accompanied by a lowering of $\Delta\mu_{\mathrm{In}}$ (*dotted lines*). The unconstrained chemical potential (*solid line*) shows an abrupt drop at the growth transition

material from the wetting layer. Consequently, the thickness of the wetting layer after completed quantum dot growth is typically smaller than its critical thickness required for the onset of quantum dot nucleation [46, 47]. This phenomenon is clearly observable for SiGe quantum dots on Si, where STM images show a ring-shaped depleted zone around the quantum dots [62]. For InAs quantum dots on GaAs, experimental evidence for material uptake has been found as well (following its theoretical prediction in [47]), both indirectly (from an analysis of the total volume of the islands formed [63]), and directly from inspection of STM images of quantum dots grown near steps [64–66]. For the modeling, this means that another energy contribution stemming from the thinning of the wetting layer has to be added to the energy balance of the hybrid approach, if we are to correctly describe the evolution of a quantum dot ensemble. This third contribution—that adds to the elastic and the surface energy contribution—rises as the quantum dots grow larger (see Fig. 1.10(a)). Consequently, there is a minimum in the energy per volume for an ensemble of identical quantum dots in equilibrium with the wetting layer. In [47], an identical shape (a truncated pyramid) and size of the quantum dots has been assumed for the sake of simplicity. With the density of 3D island nucleation $n_{3\mathrm{D}}$ as input, this theory enables us to predict the size reached by the quantum dots for any given amount θ_0 of deposited material. As shown in Fig. 1.10(b), the results are in good agreement with experimental observations.

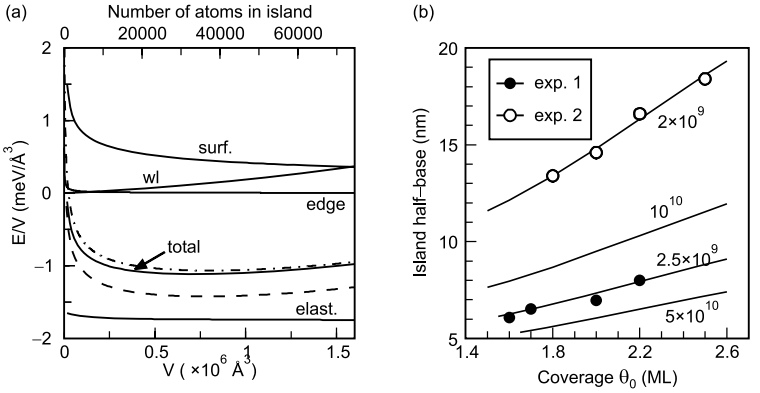

Fig. 1.10. (**a**) Total energy gain per volume due to island formation for an ensemble of identical islands in equilibrium with a wetting layer, according to the hybrid approach. Various energy contributions (*solid lines*) are shown for an island density of $n_{3D} = 10^{10}$ cm^{-2} and indium deposition $\theta_0 = 1.8$ ML. The dashed line is the total energy gain for $n = 10^{10}$ cm^{-2}, $\theta_0 = 1.5$ ML. (**b**) Dependence of the final size of the quantum dots, expressed by half of their base length, on the amount of InAs deposited (coverage θ_0) assuming various island densities (labels in cm^{-2}). The experimental values are taken from [67] (•) and estimated from [68] (○)

For unequal sizes of the quantum dot nuclei, the theory needs to be extended to include the kinetics of quantum dot growth. It can be shown (see Sect. 1.4.4) that dense metastable arrays of quantum dots kinetically evolve into a sharply peaked size distribution due to the repulsive interaction between quantum dots. Direct insight into the temporal evolution of quantum dots can be obtained from kMC simulations. This requires us to include the effect of strain on the interaction between islands and adatoms in the energy functional governing the kMC simulations. In this way, it has been possible to follow the evolution of 2D platelets that can be considered the starting point of subsequent 3D island growth [69, 70]. As a result of these simulations, it has been observed that the narrow size distribution of the platelets is accompanied by spatial ordering, where platelets align either in chains [71] or arrays [72] oriented along elastically soft directions. These growth simulations have been used as input for a realistic modeling of transport features like capacitance-voltage characteristics [73]. Another example for the use of kMC simulations is the investigation of Si micro-crystal nucleation inside droplets of liquid indium [74] where micro-crystals of pyramidal shape develop. Transitions between vertically correlated and anticorrelated growth of self-organized quantum dot stacks have also been studied by kMC simulations [75].

Studies of the growth of quantum dots by material transport on the wetting layer require detailed knowledge about the underlying microscopic diffusion processes. With this motivation, the energy barriers for hopping of In adatoms have been investigated by DFT calculations, both for the GaAs(001)$c(4 \times 4)$ surface [18] initially present before In deposition, as well as for an alloyed wetting layer surface, terminated by an $In_{2/3}Ga_{1/3}As$ layer in (2×3) or (1×3) reconstruction [19].

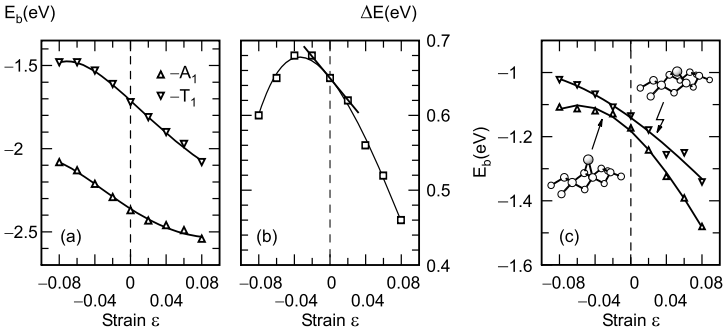

Fig. 1.11. (**a**) Binding energy E_b as a function of isotropic strain ϵ for an indium adatom at the stable binding site $\boldsymbol{A}_1$, and at the energy barrier for surface hopping, $\boldsymbol{T}_1$. (**b**) Diffusion barrier $\Delta E \equiv E_b(\boldsymbol{T}_1) - E_b(\boldsymbol{A}_1)$ as a function of ε. Full curves on both panels represent least-squares polynomial fits to the calculated points. (**c**) Binding energy of an indium adatom for the depicted bonding configurations, inside or outside As dimers, as a function of strain

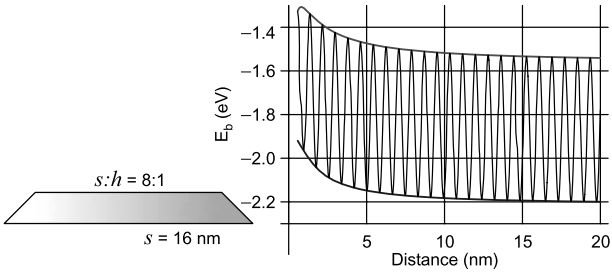

Fig. 1.12. Energy profile (*oscillating curve*) for an In adatom approaching perpendicular to a very long, coherently strained InAs island (of width s and height h) on the $c(4 \times 4)$-reconstructed GaAs(001) surface. Superimposed on the diffusion potential due to the atomic structure of the surface, the strain field in the substrate induced by the island has a repulsive effect that lifts both the binding energies (*thick lower line*) and transition state energies (*thick upper line*) close to the island

It was found that even at low island density, when the quantum dots are far apart and do not interact directly, the strain field induced in the substrate may affect material transport. This, in turn, leads to an indirect interaction between growing quantum dots competing for deposited adatoms. For the example of In diffusion on the GaAs(001)$c(4 \times 4)$ surface, DFT calculations could show that the compressive strain induced by the quantum dot in the surrounding substrate may hinder material transport considerably [18, 25], because compressive strain lowers the binding energy of In adatoms and raises the energy barrier for diffusion (at least for moderately negative strain values, see Fig. 1.11(b)). By combining the DFT results with information about the local strain field around an island obtained from elasticity theory within the flat-island approximation, it is possible to map out the potential energy profile for In diffusion on length scales that are large compared to the atomic scale. As shown in Fig. 1.12, a repulsive wall is built up around the island. If two islands compete for

deposited material, this strain effect on the diffusion will allow the smaller island to collect more adatoms and thus to catch up with the larger island when further material is deposited. This mechanism offers an explanation for the narrow island size distributions attainable experimentally even for low island densities that preclude direct elastic interactions between the islands.

1.4 Thermodynamics and Kinetics of Quantum Dot Ensembles

1.4.1 Equilibrium Volume of Strained Islands versus Ostwald Ripening

Growth interruption or annealing is frequently used as a part of the technological process to let a system come to—or at least closer to—equilibrium. Under typical experimental conditions, evaporation of atoms and intermixing/segregation are negligible, and the heteroepitaxial system evolves toward a constraint *surface equilibrium*. This is the equilibrium theory of heteroepitaxial growth. The latter traditionally distinguishes three growth modes: *i*) Frank–van-der-Merwe, or layer-by-layer growth; *ii*) Volmer–Weber, or three-dimensional (3D) island growth; and *iii*) Stranski–Krastanov growth, where a flat wetting layer is formed first and 3D islands are formed when the wetting layer reaches a critical thickness.

Here we focus on the Stranski–Krastanow growth regime, which is realized in semiconductor systems of major interest, like Ge/Si and InAs/GaAs. If the amount of deposited material is below 1 monolayer, an array of monolayer-high, two-dimensional islands forms. For a dilute array of islands, the energy of formation of a single island consisting of N atoms is given by

$$E(N) = -WN + C_1\sqrt{N} - C_2\sqrt{N}\ln\left(\sqrt{N}\right). \tag{1.2}$$

The first term is the binding energy between the atoms in the adsorbate layer, and the second term is the island edge energy due to broken chemical bonds. The third term is the elastic relaxation energy associated with the discontinuity of the surface stress tensor at the island boundaries [76–79].

The energy per atom, $\varepsilon(N) = E(N)/N$ is plotted in Fig. 1.13(a). It always has a minimum at the optimum size $N_0 = \exp[2(C_1/C_2) + 1]$ at which the energy per atom is lower than in a fully ripened island ($N \to \infty$) by the quantity $\varepsilon_0 = C_2 N_0^{-1/2}$, which demonstrates the existence of an equilibrium volume of a 2D island.

Direct experimental proofs of quantum-dot behavior of flat monolayer-high islands have been obtained for 1–2 monolayer-high CdSe insertions in ZnSSe matrix from spot-focused cathodoluminescence studies [80] as well as from photoluminescence studies of the islands in small etched mesas [81]. One of the key advantages of submonolayer QDs is a possibility to obtain arrays of islands with an ultra-small size and ultra-high density. Thus, an array of submonolayer InAs/GaAs QDs has been used as an active medium in vertical-cavity surface emitting lasers (VCSELs) allowing the ultrahigh frequency (20 GB/s) thermally insensitive (up to 85°C) operation [9–11].

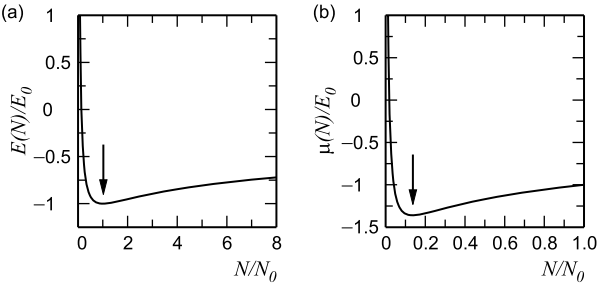

Fig. 1.13. (**a**) The energy per atom versus the volume of a 2D strained island, $E(N)/E_0$. (**b**) The chemical potential of a 2D strained island, $\mu(N) = \mathrm{d}E/\mathrm{d}N$. Arrows point on the characteristic volumes of islands, N_0, and N_1, respectively

If the amount of the deposited material exceeds the critical thickness of the wetting layer, three-dimensional islands form. Let N atoms from the wetting layer form an islands. Then the formation energy of the island can be written as follows [82]

$$E(N) = -\Delta E_{\mathrm{elast}} N + \Delta E_{\mathrm{surf}} N^{2/3} + \Delta E_{\mathrm{edges}} N^{1/3} - \Delta E_{\mathrm{elast}}^{\mathrm{edges}} N^{1/3} \ln\left(N^{1/3}\right). \tag{1.3}$$

The first term in (1.3) is the energy of the volume elastic relaxation due to the transition of the material from a highly strained flat wetting layer to a partially relaxed 3D strained island. The second term is the change of the total surface energy of the system due to the formation of tilted facets of the island and disappearance of the wetting layer surface beneath the island. The third term is the short-range contribution to the energy of the edges. The last, fourth term is the energy of the elastic relaxation due to surface stress tensor discontinuity at the edges [83, 84].

The first and the fourth terms in (1.3) are always negative, and the third term is always positive. The second term, the change of the surface energy given by the second term, can be written for a particular square-base pyramidal shape as follows [85]

$$\Delta E_{\mathrm{surf}} = (6 \cot\theta_0 v)^{2/3}\left[\gamma(\theta_0)\sec\theta_0 - \gamma_{\mathrm{WL}} - g_1(\theta_0)\tau\varepsilon_0 - g_2(\theta_0)S\varepsilon_0^2\right]. \tag{1.4}$$

Here ϑ_0 is the tilt angle of the side facets, v is the unit cell volume, $\gamma(\theta_0)$ is the surface energy of the side facets, γ_{WL} is the surface energy of the wetting layer, ε_0 is the lattice mismatch between the deposited material and the substrate, the third and the fourth terms are strain-induced renormalization terms in the surface energy, τ is a typical value of the surface stress, S is a typical value of the second-order elastic moduli of the surface, and g_1 and g_2 are geometrical factors. A key point is that ΔE_{surf} can be both positive and negative.

In an array of 3D islands, the substrate-mediated elastic interaction energy contributes to the total energy of the island array. To address the question of the minimum energy state of an array of 3D islands on a wetting layer surface, it is convenient to consider an array of equal-volume and equal-shape pyramids. Assume the total

number of atoms in the islands is fixed and the island shape is fixed, then seek the minimum energy per atom. The energy per atom versus the island volume N equals

$$\frac{E(N)}{N} = -\Delta E_{\text{elast}} + E_0\left[\frac{2\alpha}{e^{1/2}}\left(\frac{N_0}{N}\right)^{1/3} - \frac{2}{3}\left(\frac{N_0}{N}\right)^{2/3}\ln\left(\frac{e^{3/2}N_0}{N}\right) + \frac{4\beta}{e^{3/4}}\left(\frac{N_0}{N}\right)^{1/2}\right]. \tag{1.5}$$

Here $N_0 = \exp[3(\Delta E_{\text{edges}}/\Delta E_{\text{elast}}^{\text{edges}} + 1/2)]$ is the equilibrium island volume for the particular case $\Delta E_{\text{surf}} = 0$. The value $E_0 = (1/2)\Delta E_{\text{elast}}^{\text{edges}} N_0^{-2/3}$. The value $\alpha = e^{1/2}\Delta E_{\text{surf}}/\Delta E_{\text{elast}}^{\text{edges}}$ is the ratio of the change of the surface energy due to the formation of islands, ΔE_{surf}, and of the contribution of the edges to the elastic relaxation energy. The value β is the ratio of the average interaction energy between the islands, and $\Delta E_{\text{elast}}^{\text{edges}}$, it increases upon coverage q as $q^{3/2}$ [82].

Figure 1.14(a) shows the energy per atom, $E'(N) = E(N)/N + \Delta E_{\text{elast}}$ versus the island volume N in a dilute limit, where the elastic interaction between islands is neglected. For clarity, the energy versus $N^{1/3}$ is plotted. It can be seen that, if $\alpha < 0$, there exists a finite island size corresponding to the minimum of the energy per atom; the minimum is governed by the strain-induced renormalization of the surface energy. An interval of α where $0 < \alpha < 1$, the energy per atom minimum at a finite island size is due to the surface stress relaxation at the island edges. If $\alpha > 1$,

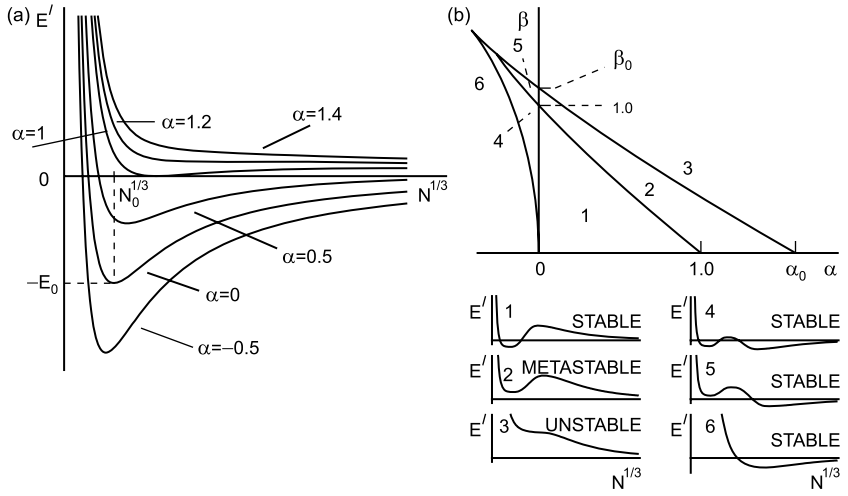

Fig. 1.14. (**a**) Energy per atom versus island volume in a dilute array of 3D strained islands. (**b**) Phase diagram of an array of elastically interacting 3D strained islands. The parameter α is the ratio of the change of the surface energy due to the formation of islands, ΔE_{surf}, and of the contribution of the edges to the elastic relaxation energy, $|\Delta E_{\text{elast}}^{\text{edges}}|$. The parameter β is the ratio $E_{\text{inter}}/|\Delta E_{\text{elast}}^{\text{edges}}|$

the island array exhibits a thermodynamic driving force to Ostwald ripening, where all material should be ultimately collected in one huge island. Practically ripening results in the formation of huge islands, where defects form. If the density of islands increases, the elastic interaction between islands mediated by the substrate becomes an important contribution to the energy per atom in the array of islands. This is a positive energy of elastic repulsion that favors ripening. Figure 1.14(b) shows an equilibrium phase diagram. A stability region implies that an array of equal-size islands is the minimum energy state of the system. In a region of metastability a thermodynamic driving force to ripening exists, but an array of equal-size islands may occur as a metastable state. In a region of instability no metastable state is possible, and an array of islands will ripen.

In a real system, the constraint surface equilibrium implies, that islands and the wetting layer can exchange atoms, and the total number of atoms is fixed in the combined system "islands plus wetting layer". The equilibrium phase diagram is more complex but still contains parameter regions of equal-volume islands, where ripening is not thermodynamically favorable [86]. This conclusion persists [87] if one also takes into account the change of the island shape upon volume increase, similar to one discussed earlier in Sects. 1.3.1 and 1.3.2.

By changing control parameters of a system, it is possible to drive an array of islands from a stable state to an unstable one which results in ripening. For III–V heteroepitaxial systems, such control can be realized, e.g., by changing the arsenic pressure in the vapor [88–90]. Existence of thermodynamically stable ensembles of the islands can be confirmed by reversible changes of islands density, volume and the wetting layer thickness upon cycled temperature ramping and cooling [91, 92]. At the same time an array of islands can also be formed as an intermediate state of the ripening process. Experimental tools that allow us to distinguish kinetically dominated arrays of islands from thermodynamically dominated ones are discussed in detail in [87]. One of the tools is described in Sect. 1.4.2.

The minimum energy per atom (MEA) attained for islands of a certain finite volume corresponds to the equilibrium volume at $T = 0$. Upon temperature increase, the equilibrium distribution of islands shows broadening and a shift of the distribution function maximum toward smaller volumes [93]. At higher temperatures, a second maximum evolves in the distribution function due to the gas of single adatoms. Finally, the distribution function maximum corresponding to nanoscale islands disappears and the distribution function becomes monotonically decreasing. A key feature of the equilibrium island distribution that can be observed experimentally is a decrease of the average island volume upon temperature increase.

1.4.2 Crossover from Kinetically Controlled to Thermodynamically Controlled Growth of Quantum Dots

As a relatively narrow volume distribution of the islands can be both a thermodynamically stable state of the system and an intermediate kinetically controlled state, it is of major interest to establish experimental tools that would allow us to distinguish between the two cases.

To address this issue, a kinetic Monte Carlo (kMC) simulation of the formation of two-dimensional strained islands upon growth interruption has been carried out. The growth simulations of [94] use an event-based algorithm applied to a solid-on-solid model with deposition and diffusion as the relevant processes. Diffusion of adatoms occurs on a square lattice by nearest neighbor hopping. Atoms can cross island edges by surmounting a Schwöbel barrier. The relevant energies in our simulations are the binding energy to the surface $E_s = 0.7\,\text{eV}$ and the strength of the $n \leq 4$ nearest neighbor bonds $E_b = 0.3\,\text{eV}$ that influence the time scale for diffusion and island formation, respectively. Existing islands generate an elastic strain field caused by the lattice mismatch. This strain field influences detachment from island boundaries and the motion of adatoms in the vicinity of islands through a position-dependent energy correction term E_{str}.

The hopping rate for a single atom is then given by an Arrhenius law

$$p = \nu \exp\left[-\frac{E_s + nE_b - E_{str}}{k_B T}\right], \tag{1.6}$$

with the attempt frequency $\nu = 10^{13}\,\text{s}^{-1}$, and the strain energy density has been calculated using Green's function approach and the normalized per atomic bond.

The simulations have been performed on a lattice of 250×250 atomic sites. As an initial step a coverage of 4% was deposited randomly on the surface at a flux of 1 ML/s. Every 0.01 s a histogram of the island size distribution is recorded. To reduce the noise, ten simulations with different initial conditions have been used to calculate an average. Figure 1.15 displays the simulation results for the temporal evolution of an average island size $< \sqrt{N} >$ for temperatures of $T = 675\,\text{K}$, 700 K and 725 K.

From Fig. 1.15 it is evident that in the initial stages of island growth the size distribution is clearly kinetically controlled. At lower temperatures many small islands are formed whereas at higher temperatures fewer and larger islands emerge.

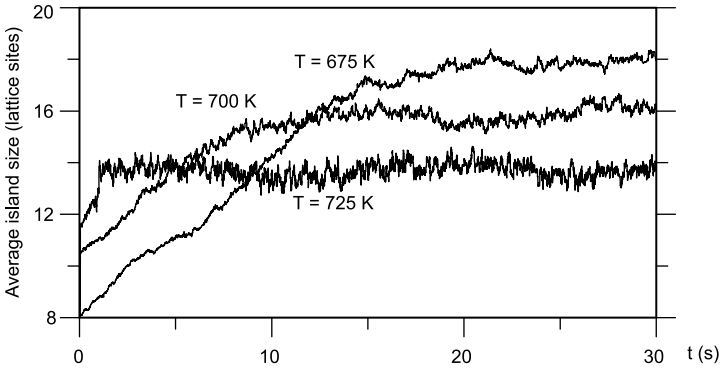

Fig. 1.15. Temporal evolution of the average island size for $T = 675\,\text{K}$, $T = 700\,\text{K}$, and $T = 725\,\text{K}$. Monte Carlo simulations have been performed on a 250×250 grid and averaged over ten runs with the same set of parameters

On short time scales of a few seconds the islands do not grow by a considerable amount and the scaling of the island size with temperature is still kinetically controlled.

At lower temperatures the nucleation of islands is the dominant process. Since the adatom mobility is low, the density of single adatoms increases fast during the deposition and pairs of atoms are formed randomly. Those act as nuclei for islands. Consequently, one observes many small islands for low temperatures.

With increasing temperature the adatoms become more and more mobile. A single adatom in a hot system can travel a long distance until it finds an existing island to which it will attach. The adatom density therefore decreases and nucleation of new islands is suppressed. The final spatial configuration in the kinetically controlled regime exhibits few large islands.

Right after the deposition, however, the islands begin to equilibrate. The system is now in an intermediate state between kinetically and thermodynamically controlled growth conditions. The slow increase of island sizes and a crossover of the average island size for systems of different temperatures is a characteristic of this regime.

For low temperatures the growth process is the slowest and the higher the temperature becomes the faster the islands approach their average equilibrium size. Once the equilibrium size distribution is reached, the average island diameter remains constant. In the course of equilibration the islands in the low temperature systems continue to grow until they reach their equilibrium size at an average diameter above that of the islands of the hotter systems, as is expected for islands grown under equilibrium conditions.

From the results of the thermodynamic theory and of the kinetic simulations, an experimental tool emerges that allows us to distinguish between kinetically controlled islands and thermodynamically controlled islands. If, upon increase of the substrate temperature, an average number of atoms in the islands, or the average island volume increases, the island formation is controlled predominantly by the growth kinetics. If, with increasing of the substrate temperature, the average island volume decreases, the island formation is controlled predominantly by thermodynamics. For submonolayer islands, the height is fixed, and the island volume is proportional to the square of the island lateral size, thus the above arguments apply to the dependence of the lateral size vs. temperature.

This developed method has been used to analyze an array of submonolayer (0.3 ML) InAs islands on GaAs substrate. Two structures of InAs islands deposited at two different substrate temperatures, 350°C and 480°C have been capped by GaAs and studied by cross-section high-resolution transmission electron microscopy (HRTEM) and photoluminescence (PL) [95], see also [2]. Cross-sectional HRTEM images processed by using DALI (digital analysis of lattice images) evaluation program (see, e.g. [96]) have revealed local map of the vertical lattice parameter, showing higher values of the latter in the regions with higher In content. HRTEM has indicated smaller islands in the sample grown at the higher temperature. PL spectra referring the entire ensemble of islands have revealed a blue shift of the QD peak in the sample grown at a higher temperature confirming a larger volume of the islands. Thus, the higher the substrate temperature during island formation, the smaller the

average volume, which indicates that the array of strained islands is predominantly thermodynamically controlled.

1.4.3 Tunable Metastability of Quantum Dot Arrays

The energetics of an array of strained islands, namely the existence of an energetically preferred island volume, makes a strong impact on the ensemble evolution kinetics even at island volumes far below the preferred one. The behavior is similar for 2D (monolayer-high) islands and for 3D islands with a strain-renormalized surface energy. For simplicity 2D islands have been considered in detail. For a dilute array of islands, the energy of formation of a single island consisting of N atoms is given by (1.2). The chemical potential of the island is given by $\mu = \mathrm{d}E(N)/\mathrm{d}N$, which is displayed in Fig. 1.13(b) and has a minimum at $N_1 = N_0/e^2 \approx 0.14N_0$.

The time evolution of the island volume distribution function $f(t, N)$ can be described by a Fokker–Planck equation,

$$\frac{\partial}{\partial t} f(t, N) = -\frac{\partial}{\partial N} J(t, N), \tag{1.7}$$

where the flux in the configurational space of island volume is

$$J(t, N) = \omega(N)\left[\frac{\bar{\mu} - \mu(N)}{k_\mathrm{B}T} f(t, N) - \frac{\partial}{\partial N} f(t, N)\right]. \tag{1.8}$$

Here the typical case is considered where the kinetics are limited by attachment (detachment) process to (from) island perimeter and the kinetic factor $\omega(N) = N^{1/2}$. The first term in (1.8) is conventionally referred to as the drift contribution and is proportional to the difference between the chemical potential $\mu(N)$ of an island having N atoms and that of the adatom sea, $\bar{\mu}$. The second term is known as the diffusion contribution. The time-dependent, mean field chemical potential $\bar{\mu}$ is determined by the mass conservation law which, in the absence of nucleation of new islands, yields the relationship between the island flux $J(t, N)$ integrated over all islands, and the deposition flux Φ,

$$\int_0^\infty J(t, N)\,\mathrm{d}N = \Phi. \tag{1.9}$$

Figures 1.16(a) and (b) show the results [61, 97] of the numerical solution of (1.7)–(1.9) under conditions of annealing, or growth interruption. The temperature is defined in units of $\Theta = C_2\sqrt{N_0}/k_\mathrm{B}$ corresponding to the energy of an island containing N_0 atoms of energy per atom ε_0. In all calculations we use $T/\Theta = 10^{-3}$ and $C_1/C_2 = 3.27$ diving $N_0 = 5.1 \times 10^3$. The initial distribution of islands is below the value N_1, and the initial evolution shown in Fig. 1.16 is governed by the negative gradient in $\mu(N)$ and, as such, is similar to conventional capillarity-driven ripening, in which the chemical potential decreases monotonically. Small islands with a chemical potential above $\bar{\mu}$ shrink, and large islands, with a chemical potential below $\bar{\mu}$, grow. The island distribution broadens and evolves to larger volumes as shown in Fig. 1.16(b).

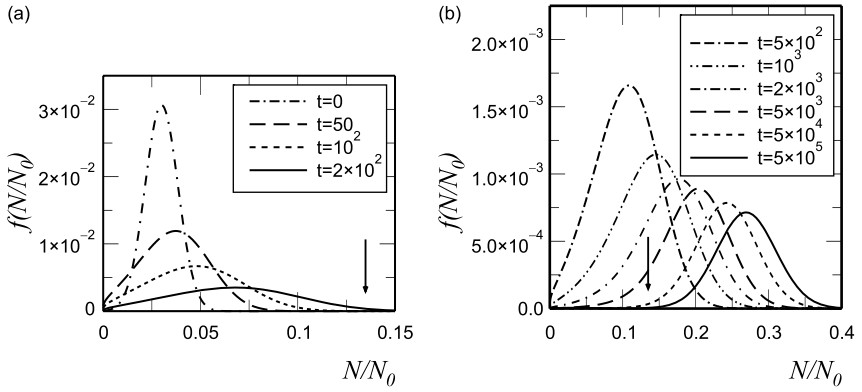

Fig. 1.16. (**a**) Early and (**b**) late evolution of the island volume distribution function $f(t, N)$ with time (scaled units) for a Gaussian initial distribution located below N_1. The solid arrow indicates the chemical potential minimum at N_1

Figure 1.16(b) shows the same island distribution evolved to larger times. The distribution passes the volume of the minimum chemical potential N_1 and at later times (say, at $t = 5 \times 10^5$) lies essentially above N_1. The following evolution of the island distribution is governed by a positive chemical potential gradient, $\mathrm{d}\mu/\mathrm{d}N > 0$. Then small islands with a chemical potential below $\bar{\mu}$ grow, and large islands, with a chemical potential above $\bar{\mu}$, shrink. The drift term in (1.7) is responsible to *inverse ripening* narrowing the island distribution. The narrowing is opposed by the diffusion term, and the two contributions to the flux J nearly cancel each other. This cancellation of terms produces a metastable state which can effectively suppress the evolution of $f(t, N)$ on experimentally relevant time scales.

Metastable states should play an important role in any kinetics of the surface nanostructures provided that positive gradients in chemical potential exist with respect to island size. Therefore, if material is deposited such that $\bar{\mu}$ is only slightly enhanced by the deposition flux, the island size distribution will be dominated by the metastable state at that particular coverage. In regions of positive chemical potential gradient, the size distribution can then be tuned to a desired size by depositing material for a required time. This "close-to-equilibrium" procedure is illustrated in Fig. 1.17 in which a uniform initial distribution of the islands between $N = 0$ and $N = 0.07N_0$ ($< N_1$) is chosen to mimic the early stages of island nucleation. For times smaller than $t = 10^3$, the deposition has little effect and the evolution is similar to the annealing case (Fig. 1.17(a)). The distribution becomes metastable as it passes above N_1 and further flux causes the Gaussian-like state to drift to higher volumes with only a slight broadening of the profile (Fig. 1.17(b)).

Within the interval of island volumes with a positive chemical potential gradient leads, many metastable states are possible with a different average volume. Depositing material by a small flux or using a two-stage (growth and annealing) procedure, it is possible to effectively tune metastable states. Similar behavior occurs for 3D

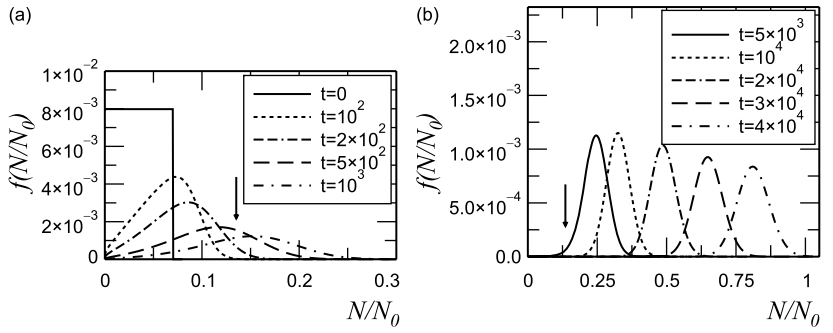

Fig. 1.17. (**a**) Early and (**b**) late evolution of the island volume distribution function $f(t, N)$ with time (scaled units) for a uniform initial distribution located below N_1 in the presence of a small deposition flux. The solid arrow indicates the chemical potential minimum at N_1

strained islands with the strain-renormalized surface energy, which have the minimum energy per atom volume [98]. The predicted kinetics of the ensemble evolution is in agreement with the experimental observations of Fe islands on NaCl(001) substrate (magnetic quantum dots) performed by atomic force microscopy (AFM) [99].

1.4.4 Evolution Mechanisms in Dense Arrays of Elastically Interacting Quantum Dots

In dense arrays of islands, where the average distance between islands is comparable with their base length, the elastic interaction energy between the islands becomes important. As discussed Sect. 1.4.1, the elastic interaction energy on the average is the positive energy of elastic repulsion. Therefore it reduces the domain of the phase diagram [82] corresponding to a stable array of the equal-size islands and favors ripening, or coarsening.

Elastic interaction takes on a completely different role with local variations in the strain field in dense arrays of islands. This role can be most easily elucidated on a model example of an array of strained islands having a conical shape [61, 100]. The total energy of the island array is then given by the formula

$$E_{\text{total}} = \frac{3}{2}\beta V_a^{2/3} - wJ\tan\vartheta V_a + \frac{w}{\pi}\sum_{b\neq a}\frac{V_a V_b}{R_{ab}^3}F\left(\frac{\rho_a}{R_{ab}}, \frac{\rho_b}{R_{ab}}\right), \tag{1.10}$$

where the first term represents the additional surface energy associated with the island formation. The second term is the elastic self-relaxation energy of the island, and the third term represents the elastic interaction energy between the ath island and all other islands. Here V_a and ρ_a are the respective volume and the base radius of the ath cone and R_{ab} is the distance between the basal centers of islands a and b. In the coefficient $w = (1+\nu)(1-\nu)^{-1}Y\varepsilon_0^2$, where ε_0 is the lattice mismatch between the deposit and the substrate, Y and ν are Young's modulus and Poisson's ratio, respectively, assuming both materials are equal, and the numerical factor $J = 1.059$.

The coefficient $\beta = 2\pi^{1/3}3^{-1/3}(\cot\vartheta)^{2/3}(\Delta\Gamma)$, where $\Delta\Gamma = \gamma(\vartheta)\sec\vartheta - \gamma(0)$ and $\gamma(\vartheta)$ and $\gamma(0)$ are the surface energies of the tilted surface of the island and of the flat surface of the wetting layer, respectively. The role of local elastic interactions is more pronounced in the case where $\Delta\Gamma > 0$ so that, even without elastic interactions, islands would tend to ripen to reduce the overall surface energy.

Now we can discuss the evolution of an array of islands in the regime of attachment-limited kinetics. Islands can attach atoms from the adatom sea and detach atoms which go to the adatom sea. The local flux of atoms to/from each island is governed by the local difference between the chemical potential of an atom, μ_a and the adatom sea, $\bar{\mu}$,

$$\frac{\mathrm{d}V_a}{\mathrm{d}t} = V_a^{1/3}[\bar{\mu} - \mu_a], \tag{1.11}$$

where the chemical potential of an island is defined as $\mu_a = \partial E_{\text{total}}/\partial V_a$. The elastic interaction energy between the two conical islands has been calculated exactly in [102]. The key feature of this energy is that its contribution to the chemical potential *diverges* as two islands nearly contact each other.

To emphasize the impact of the elastic interaction on the evolution of a dense array of islands, an initially hexagonal array of identical conical islands was considered, and an initial perturbation in island volumes and positions was introduced. Figures 1.18(a) and 1.18(b) compare the evolution of island radii without strain and with strain included. The evolution of a dense array of islands without strain is dominated by the coalescence events, when two islands touch each other and form a single island by adding up their volumes. The coalescence events manifest themselves as abrupt jumps in island radii. When the strain is included, no abrupt jumps occur. The latter means that no coalescence on impact occur in an array of strained islands, and the coarsening proceeds via the Ostwald ripening mechanism. Thus,

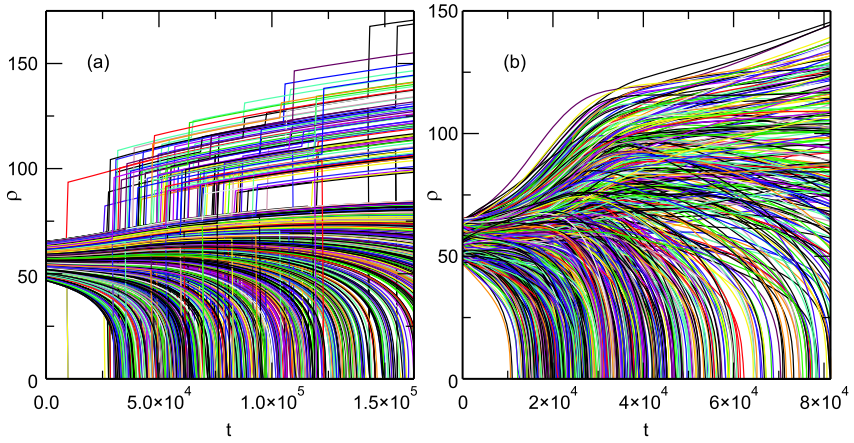

Fig. 1.18. Time evolution for the scaled radii ρ for the initial arrays shown in (**a**) for zero strain and (**b**) with strain included

a dramatic increase of the chemical potential of a strained island in the vicinity of another strained island due to local strain fields suppresses the coalescence. In addition, the elastic interaction alters the temporal behavior of the average density and radius of the islands, which is in agreement with the experimental data on dense arrays of GeSi/Si islands [103].

In ultra-dense arrays, where islands nearly touch each other, a metastable state may occur, which is stable against small perturbations in island volumes and positions [100, 104]. Thus, surprisingly, a positive elastic energy of elastic repulsion between islands can stabilize ultra-dense arrays.

1.5 Quantum Dot Stacks

Combining on the one hand self-organization phenomena providing quantum dots and quantum wires, and nanoengineering on the other, allows us to extend substantially the variety of nanostructures as well as to control their geometry and electronic spectrum. A straightforward way is to grow a multisheet array of quantum dots separated by spacers. This eventually results in the formation of multisheet arrays of quantum dots.

The growth of typical multilayer arrays of quantum dots, e.g. InAs/GaAs, Ge/Si, etc. often exhibits the formation of vertically correlated arrays, wherein the dots of the next layer are located above the dots of the previous layer forming vertical columns (see, e.g. [2] and the references therein). The vertical columns with a thin spacer result in electronic coupling of the neighboring QDs.

The advantages of using QD stacks include *i*) an enhanced volume density of QDs, resulting in a higher performance of optoelectronic devices; *ii*) engineering of electronic states in coupled QDs; and *iii*) enhancement of size homogeneity and spatial ordering.

The theoretical understanding of spatial correlation in QD stacks is based on the arguments of constraint thermodynamics. As bulk diffusion in semiconductors at typical growth temperatures is negligibly slow, the structure of the buried islands does not change during the formation of every next sheet of the islands. The islands on the surface are formed in the static strain field created by the buried islands. It has been conventionally believed that the islands of the next layer are formed at the positions of the minimum elastic energy density. This approach has explained the formation of vertical columns of QDs [105] and the enhancement of ordering in the upper layers [106].

1.5.1 Transition between Vertically Correlated and Vertically Anticorrelated Quantum Dot Growth

Surprisingly, the growth of multisheet arrays of CdSe submonolayer islands separated by ZnSe spacers has revealed anticorrelated growth, wherein the islands of the next sheet form over the spacings between the islands of a previous sheet [107].

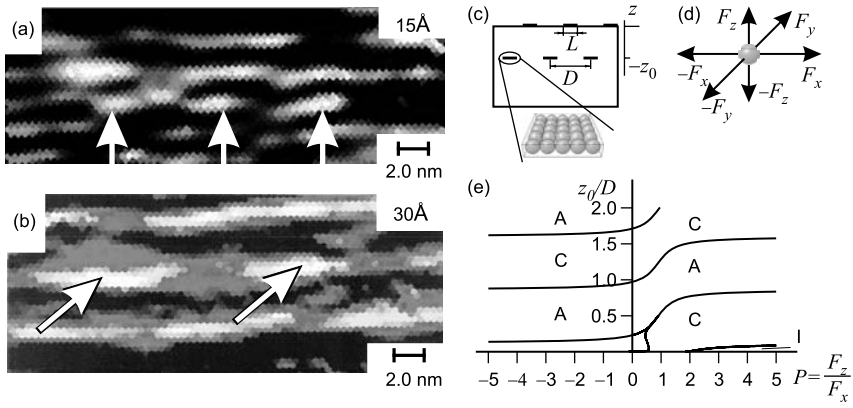

Fig. 1.19. Structure of multilayer arrays of 2D islands. (**a**)–(**b**) Processed cross-sectional high-resolution transmission electron microscopy (HRTEM) images of CdSe/ZnSe multilayer island structure. White arrows: a guide to the eye. (**a**) Spacer thickness 15 Å, vertically correlated array. (**b**) Spacer thickness 30 Å, vertically anticorrelated array. (**c**) Schematic structure of a two-layer array. (**d**) A single atom in a buried island as a dipole force source. (**e**) Diagram of a two-layer structure of 2D islands, "C" refers to a correlated array, "A" stands for an anticorrelated array, and "I" means an intermediate one

This phenomena has been explained and the theory of the formation of a multisheet array of the islands has been developed [108]. The key point is the elastic anisotropy of the semiconductors, characterized by the dimensionless parameter $\xi = (c_{11} - c_{12} - 2c_{44})/c_{44}$, where c_{11}, c_{12}, and c_{44} are elastic moduli in the Voigt notation. In Si, Ge and III–V semiconductors having the zinc-blend, structures are cubically anisotropic medium, with $\xi < 0$ and elastically soft directions $\langle 100 \rangle$. As a consequence of the anisotropy, the elastic strain field created on the surface by a periodic array of buried islands (Fig. 1.19(c)) on the surface exhibits an oscillatory decay as a function of the spacer thickness, z_0. If each of the atoms constituting a buried island is presented as an elastic dipole (Fig. 1.19(d)), the resulting structure of the surface islands depends on two parameters, the ratio of the spacer thickness to the lateral period, z_0/D, and the parameter F_z/F_x which characterizes an elementary elastic dipole. Figure 1.19(e) shows a diagram of the parameter regions, in which the two layers are either correlated or anticorrelated. For a small spacer thickness an intermediate structure is also possible. The main feature of Fig. 1.19(e) is that, with an increase of the spacer thickness, the relative structure of a double-sheet array changes from correlated to anticorrelated and back.

After the theory of transition between correlated and anticorrelated arrangement had been developed, the same material system of CdSe submonolayer islands in ZnSe matrix has revealed vertical correlation at a thinner spacer (Fig. 1.19(a)) [109]. Transition between vertically correlated and vertically anticorrelated arrangements has an important implication on the optical properties of the nanostructures. In the case of a small spacer thickness and vertically correlated arrangement, the wave function

of a localized exciton is cigar-like extended in the vertical direction; the photoluminescence from the coupled quantum dots is TM-polarized [110]. If the islands in the neighboring sheets are anticorrelated, no electronic coupling between the dots occurs and the excitons are localized in separate dots. The wave function is then extended in the lateral direction, and the photoluminescence is TE-polarized.

1.5.2 Finite Size Effect: Abrupt Transitions between Correlated and Anticorrelated Growth

Further theoretical studies—focused on the elastic interaction of buried and surface point inclusions via an elastically anisotropic matrix [111]—have shown that the minimum interaction energy occurs at a certain angle of inclination α with respect to the vertical direction, whereas $\alpha = 19°$ for Si, $\alpha = 25°$ for GaAs, and $\alpha = 33°$ for ZnSe. However, these values do not explain the experimental observations of anticorrelated arrangement of GaAlAs QDs in GaAs matrix at much larger angles of inclinations [112].

The exact theoretical consideration of the arrangements in stacks of 3D QDs was carried out in [113]. Figure 1.20 emphasizes a drastic difference in the elastic strain fields created on the surface by an array of buried point-like QDs, on the one hand, and an array of finite-size QDs on the other hand, as opposed to a single point-like QD [111]. Figure 1.20(a) shows the minima (black) and the maxima (white) of the elastic interaction energy E in the relaxed surface for a single buried point-like QD. Figures 1.20(b)–(d) refer to a periodic quadratic array of QDs with a lateral spacing of $l = 25$ l.s. (lattice sites). In a neighborhood of approximately $l/2$ around each QD the elastic properties are governed by the single point defect. Outside this region, the strain fields are overlapping. Starting with a spacer thickness of $d \approx 14$ l.s., the inclination angle α increases more and more until at $d \approx 17$ l.s. the two minima induced by two neighboring QDs meet and form a flat double minimum exactly in the middle between these QDs (Fig. 1.20(c)). With further increasing spacer thickness, the position of the double minimum remains stable and unchanged for a considerable range of d values. Finally, at $d = 31$ l.s. the minimum starts moving back to a position vertically above the QDs.

The transition of the minima from a position close to vertically above the QDs to in between the QDs is also visible in the elastic energy density profiles at $d = 10$ l.s. and $d = 25$ l.s. in Fig. 1.20(d). This indicates a transition from correlated to anticorrelated growth. From Fig. 1.20(c) one infers an inclination angle for the alignment of QDs of about $\alpha \approx 45°$ for GaAs which is in reasonable agreement with the experimentally observed value of 50° [112].

Figures 1.20(e)–(g) illustrate the influence of the shape and finite volume of the QDs. A square array of pyramids, each with a base length of 20 l.s. $\times$ 20 l.s. and a height of 5. l.s. positioned with a lateral distance of $l = 40$ l.s. is considered. Compared with an array of point-like elastic defects, there are significant differences. The inclination angle α remains unchanged. But the finite volume of the Qds results in a large range of spacer thicknesses d where the minimum is directly located above the buried structures. At a spacer thickness of about 20 l.s. the energy minimum

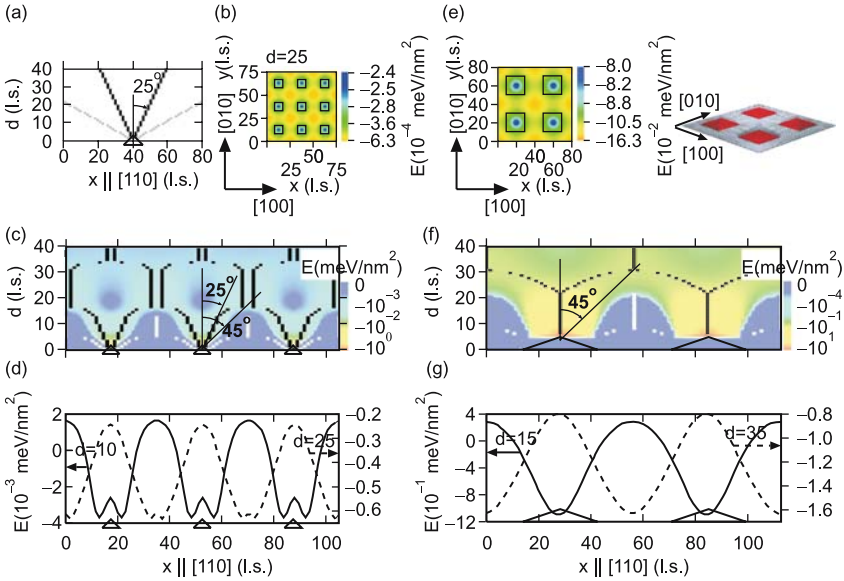

Fig. 1.20. Elastic strain field of buried strained islands in a GaAs matrix. The figure represents the strain field of one single point-like inclusion (**a**), a periodic array of point defects (**b**)–(**d**), and a periodic array of finite-size pyramids (**e**)–(**g**). (**a**), (**c**) and (**f**) show the minima (*black*) and maxima (*white*) of the elastic energy E per unit area in the [110] direction of the relaxed surface vs. spacer thickness d. (**c**) and (**f**) show $E < 0$ additionally in gray scale coding. (**b**) The density plot E in the [100]–[010] surface plane at $d = 25$. (**d**) E for $d = 10$ and $d = 25$. (**e**) The density plot at $d = 35$ (inset: 3D view). (**g**) E for $d = 10$ and $d = 35$. The positions and sizes of the buried islands are indicated by triangles [(**a**), (**c**), (**d**), (**f**), and (**g**)] and by boxes [(**b**) and (**e**)], respectively. All lengths are in units of the lattice parameter $a_{\mathrm{GaAs}} = 0.565\,\mathrm{nm}$.

splits and moves towards the anticorrelated positions between the QDs. Due to the finite size effects, the transition from the correlated to anticorrelated growth happens much more abruptly than in an array of point defects (Fig. 1.20(c)). Such an abrupt transition is indeed observed experimentally [112]. Also the double minimum of the energy profile is replaced by a single minimum (Fig. 1.20(g)). Note that the transition occurs at larger spacer thickness d for the array of QDs with a larger lateral distance of $l = 40$ l.s., and this ratio should scale for arrays with even larger lateral distance at fixed angle α. This is consistent with the experiment [112], where the transition is observed at a spacer thickness of 150 monolayers for an in-plane nearest-neighbor distance of 80–100 nm.

1.5.3 Reduction of a Size of a Critical Nucleus in the Second Quantum Dot Layer

The arguments of constraint thermodynamics that favor the formation of the QDs in the minima of the elastic energy density have allowed us to explain the spatial

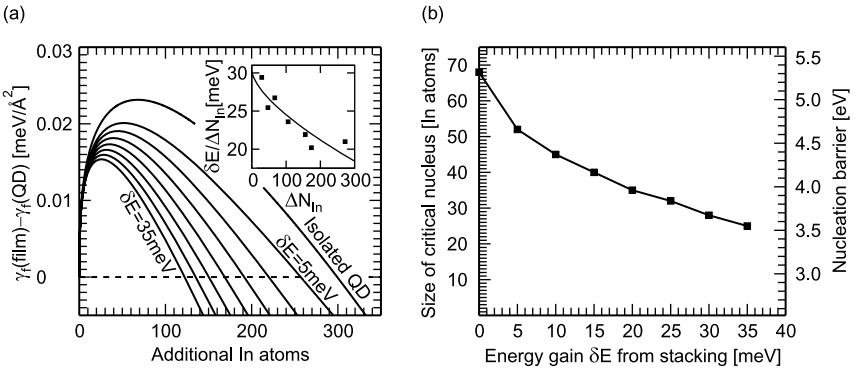

Fig. 1.21. The energy gain δE due to stacking arrangement reduces both the nucleation barriers and the size of the critical nucleus and leads to preferred nucleation above the overgrown QDs. The value of δE depends on QD shape, spacer thickness, and lateral positions with respect to overgrown QD (Fig. 1.19, Fig. 1.20)

correlations and anticorrelations in QD stacks. This approach, however, does not quantify the energetic gain for nucleation in the elastic energy density minima as compared to other nonpreferred sites. To judge the impact of the strain tensor on the surface arising from the overgrown QD as compared to possible kinetic effects, a quantitative calculation has been undertaken [114, 115] of the size reduction of the critical nucleus and lowering the nucleation barrier in the preferred nucleation site.

To consider the nucleation barrier, we focus again on the InAs/GaAs system and compare the formation energies γ_f of homogeneous InAs films of increasing thickness with QDs of increasing volume on a wetting layer of a constant thickness. The formation energy of the upper QD is lowered in the strain field

$$\gamma_f(\mathrm{QD}, N, x, y) \approx \frac{E(N)}{A} + \delta E_{\mathrm{elast}}(N, x, y) \cdot \frac{N}{A} . \tag{1.12}$$

Here $\Delta E(N)$ is the energy of the free-standing QD with no overgrown QD beneath given by (1.3), N is the number of In atoms in a QD, A is the area of the referred simulation cell, where one QD per cell is assumed. The volume dependence of $\delta E_{\mathrm{elast}} \cdot N$ is well described by a proportionality to the base area of the upper QD (inset in Fig. 1.21(a)) that senses the strain due to the overgrown QD beneath. With this result, the formation energies of hut-shaped QDs for different energy gains due to the stacking arrangement can be calculated. The obtained difference between the formation energy of a homogeneous film and a hut-shaped QD for different energy gains due to different stacking arrangements is shown in Fig. 1.21(a). The energy gain reduces the energy barrier for nucleation $\Delta\gamma_c$ and the size of the critical nucleus N_c.

Numerical calculations have revealed a linear relationship between the two y axes in Fig. 1.21(b). The critical nucleus of a free-standing QD of approximately 70 In atoms is reduced by the elastic interaction in the QD stack by up to a factor of 3 to approximately 25 In atoms (Fig. 1.21(b)) in the investigated range of energy gains δE. The energy barrier for forming the critical nucleus is lowered from $\approx$ 5.3 eV

to $\approx 3.5\,\mathrm{eV}$. The resulting increase in the nucleation rate above the overgrown QDs can thus quantitatively explain the strong tendency of the experimentally observed correlations in QD stacks. Note that the above change of $\Delta\gamma_c$ by $\approx 2\,\mathrm{eV}$ would increase the nucleation rate at a temperature of 750 K by several orders of magnitude if we assume that the rate is proportional to $\exp(-\Delta\gamma_c/k_BT)$. A weakening of the preference for perfect correlations can be due to a reduced energy gain because of, e.g., intermixing of Ga and In, or the formation of defects.

1.6 Summary and Outlook

Multiscale modeling of semiconductor nanostructures' self-organized formation has provided us with a deep insight into this broad class of exciting phenomena. Based on combination of density functional theory, multibody potentials, kinetic Monte Carlo simulations, and static continuum elasticity theory, an understanding of key aspects of the quantum dot growth has been gained.

Conclusions have been theoretically established and confirmed by careful analysis of experimental data in the following aspects of quantum dot growth.
Our investigations into quantum dots as self-organized nanostructures have revealed that:

- Gross features of quantum dot evolution are captured theoretically by constraint thermodynamic equilibrium.
- Cross-over from nucleation kinetics to thermodynamics occurs in early stages of 2D island growth.

From our study of the shape of free-standing (MBE-grown) quantum dots, we learned that:

- Shape is dominated by high-index (low-energy) facets.
- Transition to dome shape occurs due to incomplete facet growth.

Finally, our look at in-plane ordering of quantum dots led us to conclude that:

- Substrate-mediated elastic repulsion between QDs leads to ordering.
- Kinetics in dense arrays of elastically interacting QDs hinders coalescence on impact in favor of Ostwald ripening.
- Kinetics in ultra-dense arrays of elastically interacting QDs defies ripening.

Regarding 3D ordering in QD stacks:

- Alternation of vertical correlation and anti-correlation can be explained by elastic anisotropy of the matrix.

A few aspects of QD growth are still poorly understood and represent real challenges for further theoretical investigations. First, these are alloy-based QDs, like GaInAs/GaAs, SiGe/Si, etc. An alloy manifests itself not only as a material with a reduced lattice mismatch with respect to the substrate, but also represents an additional degree of freedom connected with a possible strongly inhomogeneous alloy

composition profile. The impact of possible alloy phase separation on QD formation has been pointed out in a few theoretical works (see, e.g. [116, 117]) though the understanding is far from being complete.

Second, the overgrowth (capping) of strained islands that can impose a strong change on island volume, shape, and alloy composition, is very poorly understood. Atomistic simulations of strain relaxation at different stages of InAs/GaAs QD overgrowth [118] may be considered as a first step, but more extended studies are needed.

Third, and of great technological importance, is the physics behind the defect-reduction technique, allowing efficient manipulation with threading dislocations, allowing their bending and complete blocking thus enabling growth of practically dislocation-free layers on top of heavily dislocated films [4]. Development of an adequate theory is mandatory for further technology optimization and for bringing the first examples of optoelectronic devices for the spectral region around 1550 nm on GaAs substrate to a required level for practical applications.

The authors acknowledge support from the Deutsche Forschungsgemeinschaft in the frame of the Sonderforschungsbereich 296 “Wachstumskorrelierte Eigenschaften niederdimensionaler Halbleiterstrukturen”.

References

1. D. Bimberg, M. Grundmann, N.N. Ledentsov, *Quantum Dot Heterostructures* (Wiley, Chichester, 1998)
2. V.A. Shchukin, N.N. Ledentsov, D. Bimberg, *Epitaxy of Nanostructures* (Springer, Berlin, 2003)
3. N.N. Ledentsov, in *Future Trends in Microelectronics: The Nano Millennium*, ed. by S. Luryi, J. Xu, A. Zaslavsky (Wiley, New York, 2002), p. 195
4. N.N. Ledentsov, A.R. Kovsh, V.A. Shchukin, S.S. Mikhrin, I.L. Krestnikov, A.V. Kozhukhov, L.Y. Karachinsky, M.V. Maximov, I.I. Novikov, Y.M. Shernyakov, I.P. Soshnikov, A.E. Zhukov, E.L. Portnoi, V.M. Ustinov, D. Gerthsen, P. Bhattacharya, N.D. Zakharov, P. Werner, F. Hopfer, M. Kuntz, D. Bimberg, in *Semiconductor and Organic Optoelectronic Materials and Devices*, ed. by C.-E. Zah, Y. Luo, S. Tsuji. Proceedings of SPIE, vol. 5624 (SPIE, Bellingham, 2005), p. 335
5. H.Y. Liu, S.L. Lew, T. Badcock, D.J. Mowbray, M.S. Skolnick, S.K. Ray, T.L. Choi, K.M. Groom, B. Stevens, F. Hasbullah, C.Y. Jin, M. Hopkinson, R.A. Hogg, Appl. Phys. Lett. **89**, 073113 (2006)
6. N.N. Ledentsov, A.R. Kovsh, A.E. Zhukov, N.A. Maleev, S.S. Mikhrin, A.P. Vasil’ev, E.S. Semenova, M.V. Maximov, Y.M. Shemyakov, N.V. Kryzhanovskaya, V.M. Ustinov, D. Bimberg, Electron. Lett. **39**, 1126 (2003)
7. L.Y. Karachinsky, T. Kettler, N.Y. Gordeev, I.I. Novikov, M.V. Maximov, Y.M. Shernyakov, N.V. Kryzhanovskaya, A.E. Zhukov, E.S. Semenova, A.P. Vasil’ev, V.M. Ustinov, N.N. Ledentsov, A.R. Kovsh, V.A. Shchukin, S.S. Mikhrin, A. Lochmann, O. Schulz, L. Reissmann, D. Bimberg, Electron. Lett. **41**, 478 (2005)
8. Z. Mi, P. Bhattacharya, J. Yang, Appl. Phys. Lett. **89**, 153109 (2006)
9. F. Hopfer, A. Mutig, M. Kuntz, G. Fiol, D. Bimberg, N.N. Ledentsov, V.A. Shchukin, S.S. Mikhrin, D.L. Livshits, I.L. Krestnikov, A.R. Kovsh, N.D. Zakharov, P. Werner, Appl. Phys. Lett. **89**, 141106 (2006)

10. N.N. Ledentsov, F. Hopfer, A. Mutig, V.A. Shchukin, A.V. Savel'ev, G. Fiol, M. Kuntz, V.A. Haisler, T. Warming, E. Stock, S.S. Mikhrin, A.R. Kovsh, C. Bornholdt, A. Lenz, H. Eisele, M. Dähne, N.D. Zakharov, P. Werner, D. Bimberg, Proc. SPIE **6468**, 47 (2007); Proc. SPIE Photonics West, January 21–26, 2007, San Jose, CA
11. N.N. Ledentsov, V.A. Shchukin, D. Bimberg, in *Future Trends in Microelectronics: Up the Nano Creek*, ed. by S. Luryi, J. Xu, A. Zaslavsky (Wiley, New York, 2007)
12. A.J. Bennett, D.C. Unitt, P. Atkinson, D. Ritchie, A.J. Shields, Opt. Express **13**, 50 (2005)
13. A. Lochmann, E. Stock, O. Schulz, F. Hopfer, D. Bimberg, V.A. Haisler, A.I. Toropov, A.K. Bakarov, A.K. Kalagin, Electron. Lett. **42** (2006)
14. R.M. Stevenson, R.J. Young, P. Atkinson, K. Cooper, D.A. Ritchie, A.J. Shields, Nature **439**, 179 (2006)
15. D.D. Vvedensky, J. Phys.: Condens. Matter **16**, R1537 (2004)
16. T. Hammerschmidt, Ph.D. thesis, Fritz-Haber-Institut der Max-Planck Gesellschaft. http://w3.rz-berlin.mpg.de/~hammer/Diss/Diss-ThomasHammerschmidt.pdf
17. A. Kley, P. Ruggerone, M. Scheffler, Phys. Rev. Lett. **79**, 5278 (1997)
18. E. Penev, P. Kratzer, M. Scheffler, Phys. Rev. B **64**, 085401 (2001)
19. E. Penev, S. Stojković, P. Kratzer, M. Scheffler, Phys. Rev. B **69**, 115335 (2004)
20. C.G. Morgan, P. Kratzer, M. Scheffler, Phys. Rev. Lett. **82**, 4886 (1999)
21. P. Kratzer, C.G. Morgan, M. Scheffler, Phys. Rev. B **59**, 15246 (1999)
22. C.T. Foxon, B.A. Joyce, Surf. Sci. **64**, 293 (1977)
23. P. Kratzer, M. Scheffler, Phys. Rev. Lett. **88**, 036102 (2002)
24. G.R. Bell, M. Itoh, T.S. Jones, B.A. Joyce, Surf. Sci. **423**, L280 (1999)
25. P. Kratzer, E. Penev, M. Scheffler, Appl. Phys. A **75**, 79 (2002)
26. P. Kratzer, E. Penev, M. Scheffler, Appl. Surf. Sci. **216**, 436 (2002)
27. L. Mandreoli, J. Neugebauer, R. Kunert, E. Schöll, Phys. Rev. B **68**, 155429 (2003)
28. M. Itoh, G.R. Bell, A.R. Avery, T.S. Jones, B.A. Joyce, D.D. Vvedensky, Phys. Rev. Lett. **81**, 633 (1998)
29. MPEG-videos of an animated growth sequence can be downloaded, for two different viewpoints, from ftp://ftp.aip.org/epaps/phys_rev_lett/E-PRLTAO-87-031152/isl-gaas-front.mpg ftp://ftp.aip.org/epaps/phys_rev_lett/E-PRLTAO-87-031152/isl-gaas-top.mpg
30. B.A. Joyce, D.D. Vvedensky, T.S. Jones, M. Itoh, G.R. Bell, J.G. Belk, J. Cryst. Growth **201/202**, 106 (1999)
31. F. Grosse, W. Barvosa-Carter, J.J. Zinck, M. Wheeler, M.F. Gyure, Phys. Rev. Lett. **89**, 116102 (2002)
32. F. Grosse, M.F. Gyure, Phys. Rev. B **66**, 075320 (2002)
33. F. Grosse, W. Barvosa-Carter, J.J. Zinck, M.F. Gyure, Phys. Rev. B **66**, 075321 (2002)
34. G.R. Bell, T.J. Krzyzewski, P.B. Joyce, T.S. Jones, Phys. Rev. B **61**, R10551 (2000)
35. J. Krzyzewski, P.B. Joyce, G.R. Bell, T.S. Jones, Surf. Sci. **482–485**, 891 (2001)
36. Y. Ebiko, S. Muto, D. Suzuki, S. Itoh, K. Shiramine, T. Haga, Y. Nakata, N. Yokoyama, Phys. Rev. Lett. **80**, 2650 (1998)
37. T.J. Krzyzewski, P.B. Joyce, G.R. Bell, T.S. Jones, Phys. Rev. B **66**, 201302(R) (2002)
38. F. Arciprete, E. Placidi, V. Sessi, M. Fanfoni, F. Patella, A. Balzarotti, Appl. Phys. Lett. **89**, 041904 (2006)
39. J.G. LePage, M. Alouani, D.L. Dorsey, J.W. Wilkins, P.E. Blöchl, Phys. Rev. B **58**, 1499 (1998)
40. A. Ohtake, J. Nakamura, S. Tsukamoto, N. Koguchi, A. Natori, Phys. Rev. Lett. **89**, 206102 (2002)
41. A. Ohtake, N. Koguchi, Appl. Phys. Lett. **83**, 5193 (2003)

42. E. Penev, P. Kratzer, M. Scheffler, Phys. Rev. Lett. **93**, 146102 (2004)
43. M.C. Xu, Y. Temko, T. Suzuki, K. Jacobi, Surf. Sci. **580**, 30 (2005)
44. J.G. Belk, C.F. McConville, J.L. Sudijono, T.S. Jones, B.A. Joyce, Surf. Sci. **387**, 213 (1997)
45. M. Sauvage-Simkin, Y. Garreau, R. Pinchaux, M.B. Véron, J.P. Landesman, J. Nagle, Phys. Rev. Lett. **75**, 3485 (1995)
46. L.G. Wang, P. Kratzer, M. Scheffler, N. Moll, Phys. Rev. Lett. **82**, 4042 (1999)
47. L.G. Wang, P. Kratzer, N. Moll, M. Scheffler, Phys. Rev. B **62**, 1897 (2000)
48. E. Pehlke, N. Moll, A. Kley, M. Scheffler, Appl. Phys. A **65**, 525 (1997)
49. N. Moll, M. Scheffler, E. Pehlke, Phys. Rev. B **58**, 4566 (1998)
50. Q. Liu, N. Moll, M. Scheffler, E. Pehlke, Phys. Rev. B **60**, 17008 (1999)
51. G. Costantini, C. Manzano, R. Songmuang, O.G. Schmidt, K. Kern, Appl. Phys. Lett. **82**, 3194 (2003)
52. Y. Temko, T. Suzuki, P. Kratzer, K. Jacobi, Phys. Rev. B **68**, 165310 (2003)
53. K. Georgsson, N. Carlsson, L. Samuelson, W. Seifert, L.R. Wallenberg, Appl. Phys. Lett. **67**, 2981 (1995)
54. J. Márquez, P. Kratzer, L. Geelhaar, K. Jacobi, M. Scheffler, Phys. Rev. Lett. **86**, 115 (2001)
55. J. Márquez, P. Kratzer, K. Jacobi, J. Appl. Phys. **95**, 7645 (2004)
56. L. Geelhaar, J. Márquez, P. Kratzer, K. Jacobi, Phys. Rev. Lett. **86**, 3815 (2001)
57. L. Geelhaar, Y. Temko, J. Márquez, P. Kratzer, K. Jacobi, Phys. Rev. B **65**, 155308 (2002)
58. P. Kratzer, Q.K.K. Liu, P. Acosta-Diaz, C. Manzano, G. Costantini, R. Songmuang, A. Rastelli, O.G. Schmidt, K. Kern, Phys. Rev. B **73**, 205347 (2006)
59. J. Márquez, L. Geelhaar, K. Jacobi, Appl. Phys. Lett. **78**, 2309 (2001)
60. F.M. Ross, J. Tersoff, R.M. Tromp, Phys. Rev. Lett. **80**, 984 (1999)
61. D.E. Jesson, T.P. Munt, V.A. Shchukin, D. Bimberg, Phys. Rev. Lett. **92**, 115503 (2004)
62. U. Denker, O.G. Schmidt, N.Y. Jin-Phillipp, K. Eberl, Appl. Phys. Lett. **78**, 3723 (2001)
63. P.B. Joyce, T.J. Krzyzewski, G.R. Bell, T.S. Jones, S. Malik, D. Childs, R. Murray, Phys. Rev. B **62**, 10891 (2000)
64. T.J. Krzyzewski, P. Joyce, G.R. Bell, T.S. Jones, Surf. Sci. **517**, 8 (2002), cf. Fig. 6
65. E. Placidi, F. Arciprete, V. Sessi, M. Fanfoni, F. Patella, A. Balzarotti, Appl. Phys. Lett. **86**, 241913 (2005)
66. M.C. Xu, Y. Temko, T. Suzuki, K. Jacobi, Surf. Sci. **589**, 91 (2005)
67. A. Polimeni, A. Patanè, M. Capizzi, F. Martelli, L. Nasi, G. Salviati, Phys. Rev. B **53**, R4213 (1996)
68. J.M. Moison, F. Houzay, F. Barthe, L. Leprince, E. André, O. Vatel, Appl. Phys. Lett. **64**, 196 (1994)
69. E. Schöll, S. Bose, Sol. State Electron. **42**, 1587 (1998)
70. M. Meixner, R. Kunert, S. Bose, E. Schöll, V.A. Shchukin, D. Bimberg, E. Penev, P. Kratzer, in *Proc. 25th International Conference on the Physics of Semiconductors (ICPS-25)*, Osaka 2000, ed. by N. Miura, T. Ando (Springer, Berlin, 2001), p. 381
71. M. Meixner, E. Schöll, M. Schmidbauer, R. Köhler, Phys. Rev. B **64**, 245307 (2001)
72. M. Meixner, R. Kunert, E. Schöll, Phys. Rev. B **67**, 195301 (2003)
73. R. Wetzler, R. Kunert, A. Wacker, E. Schöll, New J. Phys. **6**, 81 (2004)
74. M. Block, R. Kunert, E. Schöll, T. Boeck, T. Teubner, New J. Phys. **6**, 166 (2004)
75. M. Meixner, E. Schöll, Phys. Rev. B **67**, 121202(R) (2003)
76. V.I. Marchenko, A.Y. Parshin, Zh. Eksp. Teor. Fiz. **79**, 257 (1980) [Sov. Phys. JETP **52**, 129 (1980)]
77. A.F. Andreev, Pis'ma Zh. Eksp. Teor. Fiz. **32**, 654 (1980) [JETP Lett. **32**, 640 (1980)]
78. V.I. Marchenko, Pis'ma Zh. Eksp. Teor. Fiz. **33**, 397 (1981) [JETP. Lett. **33**, 381 (1981)]

79. D. Vanderbilt, Surf. Sci. **268**, L300 (1992)
80. R. Engelhardt, V. Türck, U.W. Pohl, D. Bimberg, J. Cryst. Growth **184/185**, 311 (1998)
81. T. Kümmell, R. Weigand, G. Bacher, A. Forchel, Appl. Phys. Lett. **73**, 3106 (1998)
82. V.A. Shchukin, N.N. Ledentsov, P.S. Kop'ev, D. Bimberg, Phys. Rev. Lett. **75**, 2968 (1995)
83. A.F. Andreev, Zh. Eksp. Teor. Fiz. **80**, 2042 (1980) [Sov. Phys. JETP **53**, 1063 (1981)]
84. V.I. Marchenko, Zh. Eksp. Teor. Fiz. **81**, 1141 (1981) [Sov. Phys. JETP **54**, 605 (1981)]
85. V.A. Shchukin, N.N. Ledentsov, M. Grundmann, P.S. Kop'ev, D. Bimberg, Surf. Sci. **352–354**, 117 (1996)
86. I. Daruka, A.-L. Barabási, Phys. Rev. Lett. **79**, 3708 (1997)
87. V.A. Shchukin, D. Bimberg, Rev. Mod. Phys. **71**, 1125 (1999)
88. N.N. Ledentsov, M. Grundmann, N. Kirstaedter, O. Schmidt, R. Heitz, J. Böhrer, D. Bimberg, V.M. Ustinov, V.A. Shchukin, P.S. Kop'ev, Z.I. Alferov, S.S. Ruvimov, A.O. Kosogov, P. Werner, U. Richter, U. Gösele, J. Heydenreich, in *Proceedings of the 7th International Conference on Modulated Semiconductor Structures*, Madrid, Spain, July 1995. Solid State Electron. **40**, 785 (1996)
89. K. Ozasa, Y. Aoyagi, Y.J. Park, L. Samuelson, Appl. Phys. Lett. **71**, 797 (1997)
90. F. Heinrichsdorff, A. Krost, D. Bimberg, A.O. Kosogov, P. Werner, Appl. Surf. Sci. **123/124**, 725 (1998)
91. N.N. Ledentsov, V.A. Shchukin, D. Bimberg, V.M. Ustinov, N.A. Cherkashin, Y.G. Musikhin, B.V. Volovik, G.E. Cirlin, Z.I. Alferov, Semicond. Sci. Technol. **16**, 502 (2001)
92. R. Leon, J. Wellman, X.Z. Liao, J. Zuo, D.J.H. Cockayne, Appl. Phys. Lett. **76**, 1558 (2000)
93. V.A. Shchukin, N.N. Ledentsov, D. Bimberg, in *Self-Organized Processes in Semiconductor Alloys—Spontaneous Ordering, Composition Modulation, and 3-D Islanding*, ed. by D.M. Follstaedt, B.A. Joyce, A. Mascarenhas, T. Suzuki, Symp. Proc., vol. 583 (Mat. Res. Soc., Pittsburgh, 2000), p. 23
94. M. Meixner, E. Schöll, V.A. Shchukin, D. Bimberg, Phys. Rev. Lett. **87**, 236101 (2001)
95. V.A. Shchukin, N.N. Ledentsov, A. Hoffmann, D. Bimberg, I.P. Soshnikov, B.V. Volovik, V.M. Ustinov, D. Litvinov, D. Gerthsen, Phys. Stat. Sol. (b) **224**, 503 (2001)
96. A. Rosenauer, S. Kaiser, T. Reisinger, J. Zweck, W. Gebhardt, D. Gerthsen, Optik (Stuttgart) **102**, 63 (1996)
97. T.P. Munt, D.E. Jesson, V.A. Shchukin, D. Bimberg, Phys. Rev. B **75**, 085422 (2007)
98. T.P. Munt, D.E. Jesson, V.A. Shchukin, D. Bimberg, Appl. Phys. Lett. **85**, 1784 (2004)
99. Z. Gai, B. Wu, J.P. Pierce, G.A. Farnan, D. Shu, M. Wang, Z. Zhang, J. Shen, Phys. Rev. Lett. **89**, 235502 (2002)
100. V.A. Shchukin, D. Bimberg, T.P. Munt, D. Jesson, Phys. Rev. Lett. **90**, 076102 (2003)
101. D.E. Jesson, T.P. Munt, V.A. Shchukin, D. Bimberg, Phys. Rev. B **69**, 041302 (2004)
102. V.A. Shchukin, D. Bimberg, T.P. Munt, D.E. Jesson, Phys. Rev. B **70**, 085416 (2004)
103. J.A. Floro, M.B. Sinclair, E. Chason, L.B. Freund, R.D. Twesten, R.Q. Hwang, G.A. Lucadamo, Phys. Rev. Lett. **84**, 701 (2000)
104. V.A. Shchukin, D. Bimberg, T.P. Munt, D.E. Jesson, Ann. Phys. **320**, 237 (2005)
105. J. Tersoff, C. Teichert, M.G. Lagally, Phys. Rev. Lett. **76**, 1675 (1996)
106. F. Liu, S.E. Davenport, H.M. Evans, M.G. Lagally, Phys. Rev. Lett. **82**, 2528 (1999)
107. M. Straßburg, V. Kutzer, U.W. Pohl, A. Hoffmann, I. Broser, N.N. Ledentsov, D. Bimberg, A. Rosenauer, U. Fischer, D. Gerthsen, I.L. Krestnikov, M.V. Maximov, P.S. Kop'ev, Z.I. Alferov, Appl. Phys. Lett. **72**, 942 (1998)
108. V.A. Shchukin, D. Bimberg, V.G. Malyshkin, N.N. Ledentsov, Phys. Rev. B **57**, 12262 (1998)

109. M. Strassburg, R. Heitz, V. Türck, S. Rodt, U.W. Pohl, A. Hoffmann, D. Bimberg, I.L. Krestnikov, V.A. Shchukin, N.N. Ledentsov, Z.I. Alferov, D. Litvinov, A. Rosenauer, D. Gerthsen, J. Electron. Mater. **28**, 506 (1999)
110. I.L. Krestnikov, M. Straßburg, M. Caesar, A. Hoffmann, U.W. Pohl, D. Bimberg, N.N. Ledentsov, P.S. Kop'ev, Z.I. Alferov, D. Litvinov, A. Rosenauer, D. Gerthsen, Phys. Rev. B **60**, 8696 (1999)
111. V. Holý, G. Springholz, M. Pinczolits, G. Bauer, Phys. Rev. Lett. **83**, 356 (2000)
112. X.-D. Wang, N. Liu, C.K. Shih, S. Govindaraju, A.L. Holmes Jr., Appl. Phys. Lett. **85**, 1356 (2004)
113. R. Kunert, E. Schöll, Appl. Phys. Lett. **89**, 153103 (2006)
114. R. Kunert, E. Schöll, T. Hammerschmidt, P. Kratzer, in *Proc. 28th International Conference on Physics of Semiconductors*, Vienna, Austria, July 2006, ed. by W. Jantsch, F. Schäffler (Springer, Berlin, 2006)
115. T. Hammerschmidt, P. Kratzer, unpublished
116. J. Tersoff, Phys. Rev. Lett. **81**, 3183 (1998)
117. N. Liu, J. Tersoff, O. Baklenov, A.L. Holmes, Jr., C.K. Shih, Phys. Rev. Lett. **84**, 334 (2000)
118. T. Hammerschmidt, P. Kratzer, Am. Inst. Phys. Conf. Proc. **772**, 601 (2005)

http://www.springer.com/978-3-540-77898-1

Semiconductor Nanostructures
Bimberg, D. (Ed.)
2008, XXI, 357 p., Hardcover
ISBN: 978-3-540-77898-1